Engineering Geology 375 (2026) 109193

Contents lists available at ScienceDirect

Engineering Geology

journal homepage: www.elsevier.com/locate/enggeo

Thermal fatigue, water-weakening spalling, and structural instability of Nabataean rock-cut façades☆

Giovanni B. Crosta [a,b,*], Giuseppe Dattola [a], Luca Cifeca Recinella [a], Alberto Previati [a], Serena Rigamonti [b]

[a] Dept. of Earth and Environmental Sciences, University of Milano Bicocca, Milano, Italy
[b] EG4RISK s.r.l., Milano, Italy

ARTICLE INFO

Keywords:
Rock-hewn Nabataean tombs
Hegra, Al-'Ula UNESCO heritage
Thermal spalling
Fracture mechanics
FE modelling
Infrared thermography
Capillarity
Stress corrosion

ABSTRACT

Rock-cut monumental façades of the Nabataean civilisation at Hegra (Al-'Ula, Saudi Arabia) exhibit progressive surface-perpendicular fracturing and surface-parallel spalling in a hyper-arid environment. The Case 2 lateral crack geometry, in which stress intensity increases monotonically with crack height with no arrest mechanism, and its probabilistic failure timeline have not previously been quantified for rock-cut heritage façades. This study presents an integrated assessment combining laboratory geomechanical characterisation of the Quweira Sandstone (porosity 11–22%; dry tensile strength 1.5–4.0 MPa; tensile strength reduced 20–40% by water saturation), a fracture mechanics–Monte Carlo probabilistic model, infrared thermographic field surveys, and three-dimensional finite element modelling. A two-case fracture mechanics model distinguishes inward-deepening cracks (Case 1) from lateral surface-parallel growth at fixed crack depth (Case 2). Case 2, consistent with the observed full-width fracture at 40–50 mm depth with the carved surface intact, produces a stress intensity factor that increases monotonically with crack height with no arrest mechanism. Monte Carlo simulation ($N = 15{,}000$, 2000-year horizon) yields a median façade lifetime $T_{50} = 615$ yr and T90 = 1100 yr for south-facing façades under dry conditions. Seismic toppling at accelerations as low as 0.8%g, **within the range of minor regional seismic events and anthropogenic vibrations,** is the critical detachment mechanism, not gravitational overturning. Morning condensation reduces fracture toughness K_{IC} and amplifies the Paris fatigue coefficient C, reducing Phase A duration by up to 15-fold; active capillary rise, field-observed at 0.3–1.05 m, reduces failure timescales from centuries to decades. Infrared thermography at 06:00 at tomb IGN55 reveals a 15.4 °C contrast between intact rock and thermally decoupled slab, mapping crack lateral extent ($h_{crack} \approx 1.5$–2.0m) and independently validating the calibrated effective thermal diffusivity ($D_{eff} = 2.33 \times 10^{-7} m^2 s^{-1}$). A photo-based inventory of the façades identifies crack evidence on 50 façades (53%), with Case 1 concentrated at dry upper cornices and Case 2 at moist façade bases and wings. Three-dimensional FEM of the Qasr al-Bint tomb group confirms stability under intact rock properties; failure initiates at 60% cohesion reduction under partial saturation, consistent with measured water-induced strength degradation. The probabilistic framework and infrared monitoring protocol are transferable to analogous Nabataean tombs at Petra and to rock-cut heritage in arid environments more broadly, providing quantitative thresholds for conservation monitoring and intervention.

1. Introduction

Rock-cut (rock-hewn) sites are distributed worldwide and span over 650,000 years of human activity. Their construction and long-term survival depend on favourable geologic conditions: weak outcropping rocks in stable, dry settings. These structures, which initially exploited natural hollows, evolved into complex multi-level structures through direct excavation in weak rocks like calcarenite, sandstone, tuff, pyroclastic deposits, marls, and karst limestones. Their sensitivity to external factors makes them susceptible to deterioration under changing environmental conditions (Fig. 1). Managing rock-cut sites therefore requires a detailed geological and environmental characterisation,

☆ This article is part of a Special issue entitled: 'Engineering geology and rupestrian heritage sites' published in Engineering Geology.

* Corresponding author.
E-mail address: giovannibattista.crosta@unimib.it (G.B. Crosta).

https://doi.org/10.1016/j.enggeo.2026.109193
Received 3 June 2026; Received in revised form 18 September 2026; Accepted 30 October 2026
Available online 4 November 2026
0013-7952/© 2026 The Authors. Published by Elsevier B.V. This is an open access article under the CC BY license (http://creativecommons.org/licenses/by/4.0/).

understanding of damage controls, and thorough knowledge of the physical and mechanical properties of the rocks and their transient changes (Wedekind et al., 2011).

Weathering in arid and semi-arid areas stems from intrinsic factors (e.g. lithology, mineralogy, cementation, grain size, fracturing, and salt content) that produce interconnected effects: granular disaggregation, capillary-rise-controlled salt damage, and differential thermal expansion under direct insolation. Among the typical morphologies are tafoni and alveoles (Paradise, 2013), natural arches, and yardangs, wind-abraded ridges (Goudie, 2013) developing parallel to prevailing winds in hyper-arid areas.

Non-invasive characterisation and monitoring are essential for heritage preservation. Topographic and photogrammetric surveys (McCarthy, 2014; Domej et al., 2022), geophysical methods (Cosentino et al., 2011; Martínez-Garrido et al., 2018; Mineo and Pappalardo, 2019; Orr et al., 2020), and geomechanical investigations (Hashemi et al., 2018; Meng et al., 2021; Wang et al., 2024; Domej et al., 2022; Rihosek et al., 2016) have contributed to understanding rock-hewn sites (D'Altri et al., 2023). Yet a comprehensive quantitative framework integrating rock mechanical properties, water infiltration, and long-term façade stability remains incomplete (Franzen and Mirwald, 2004; Sass and Viles, 2022). The site of Hegra (Madāʾin Ṣāliḥ, Saudi Arabia, UNESCO World Heritage, ICOMOS, 2008), with 111 Nabataean tombs in the Quweira Formation sandstone (Wahbi, 2014; Nehmé, 2015), is a major example of this challenge.

Water is a critical deterioration factor at these sites, with climate change altering its impact on stone decay (Sass and Viles, 2010, 2022; Ruedrich et al., 2011). Ponding, runoff, episodic surface floodwater, and wind-driven rain all contribute (Blocken et al., 2013; Franzoni, 2017; Franzen and Mirwald, 2004). Capillary rise, observed in the Quweira sandstone near Hegra at heights of 0.3–1.05 m (Fig. 2), affects the lower parts of rock-hewn structures. Water reduces cohesion and tensile strength, dissolves cementing agents, triggers clay swelling and micro-fracturing (Ruedrich et al., 2011), and transports salts that crystallise within pores during drying cycles, driving salt efflorescence and sub-florescence (Egartner et al., 2020). Rihosek et al. (2016, Safonov et al., 2020) observed that tomb walls subjected to reduced confinement are converted into hourglass-shaped pillars, with erosion and instability



Fig. 2. Capillary rise in the Quweira sandstone at the immediate proximity of a pool. Capillary rise varies with sandstone porosity, grain size and fractures, and oscillates between 0.3 m and 1.05 m. These values are compatible for the weathering at the tomb façades in Hegra and maximum water rise height of **2–2.5 m at the tomb façades**.

concentrated where stress magnitude is lowest. Through FEM and physical modelling, they described discontinuous recession in space and time of rock surfaces. They also demonstrated an inverse relationship between applied stress and decay rate by performing salt weathering experiments on Umm Ishrin sandstone (from Petra), finding up to four times faster degradation under unconfined conditions.

Wind abrasion by saltating sandy particles is most efficient within the same height range (Laity, 2011) as capillary rise, compounding the weakening. Continuous wetting–drying cycles render the sandstone more susceptible to all these mechanisms (Siegesmund and Durrast, 2011).

Among deterioration mechanisms, thermal stresses (Martel, 2017; Eppes and Keanini, 2017; Collins and Stock, 2016) and thermally driven spalling (contour scaling and flaking, Heinrich, 2008) deserve particular attention because they operate directly on the carved façade without requiring pre-existing structural discontinuities (do Amaral Vargas et al., 2013). Heinrich (2008) documented at Petra façade surface temperatures up to 55 °C, with diurnal ranges reaching 30 °C and



Fig. 1. Examples of damaged and endangered tomb façades in the Hegra (Madāʾin Ṣāliḥ) area. a) slope failure affecting the façade and inner chamber of a tomb, on the left (IGN41, numbering from Nehmé, 2006), and partially reused rock-slide fall niche for the construction of a post failure tomb (on the right; IGN42); b) and g) strongly damaged façade and tomb interior with evidence of water flooding, façade damage and thinning; c) inner view of a tomb and its façade with niches excavated within the inner façade wall; d) and e) view from the inside of two tombs with missing parts of the façade; f) front view of a set of tombs with evidence of erosion, façade thinning and partial collapse (fall).

heating/cooling rates of up to 10 °C h^{-1}, with south- and west-facing façades most severely affected. Surface-parallel fractures at shallow depth have been documented (Heinrich, 2008) but not yet interpreted within a rigorous fracture mechanics framework accounting for the specific crack geometry and thermal forcing. The relationship between cyclic thermoelastic stress, crack nucleation depth, and long-term slab stability, including episodic water contact and seismic triggering, remains unquantified. Infrared thermography, applied to natural rock slopes (Guerin et al., 2019) and heritage structures (Heinrich, 2008; Martínez-Garrido et al., 2018), offers a direct observational link between the thermal field and crack state but has not been used to calibrate and validate a fracture mechanics model at these sites. Collins and Stock (2016) provide the closest physical analogue, documenting Paris–Erdogan fatigue in exfoliation fractures of granitic rock. This study extends this to include a lateral growth geometry (termed Case 2 in the following), a three-phase Monte Carlo probabilistic lifetime framework to yield quantitative lifetime estimates (T_{50}, T_{90}), and the explicit coupling of moisture effects and IR thermographic validation, within a single calibrated heritage-conservation model.

This paper presents an integrated assessment combining: (i) laboratory geomechanical characterisation of the Quweira Sandstone including strength under dry and saturated conditions, capillarity, and water retention; (ii) a two-case analytical fracture mechanics model for thermal spalling with Monte Carlo probabilistic simulation over a 2000-year horizon; (iii) sensitivity analysis and explicit modelling of water–stress corrosion effects; (iv) infrared thermographic mapping and independent thermal calibration; and (v) three-dimensional FEM of one representative tomb group under excavation, weathering, and thermo-mechanical loading. Emphasis is placed on the physical representation of the observed surface-parallel crack geometry, the probabilistic characterisation of slab detachment triggers, and the identification of conditions under which short-term risk arises.

2. Geological and geomorphological setting

Hegra is located just north of Al-'Ula and is famous for its rock-hewn Nabataean tombs, architecturally and lithologically comparable to those of Petra (Jordan), both sites having been carved into Cambrian quartzitic sandstones of equivalent age and composition (Heinrich, 2008; Wahbi, 2014). At Hegra, 111 monumental tombs, 105 with a funerary chamber, of which 94 with a decorated façade (Nehmé, 2015), were excavated into the heterogeneous white, yellow to reddish sandstone of the Quweira Formation, mainly dated to the 1st century BCE and distributed in four main necropolises: Jabal al-Mahjar, Qasr al-Bint, Jabal al-Ahmar, and Jabal al-Khraymat.

The Hegra site lies within the western Arabian Shield, influenced by Red Sea rifting since ~30 Ma (Martinez and Cochran, 1988; Vincent, 2008). A Cambrian–Ordovician clastic succession (500–450 Ma) conformably overlies the Precambrian Jibalah Group basement (Weissbrod and Sneh, 2002), including the Siq (Lower Cambrian), Quweira (Middle–Upper Cambrian, ~150 m thick), and Saq formations, gently dipping north at ca. 05°/330°. At Petra, the tombs are carved into the stratigraphically equivalent Umm Ishrin Formation (Ram Group, ~500 Ma; Heinrich, 2008), confirming that both necropolises share host-rock mineralogy, pore structure, and thermoelastic behaviour. The Al-'Ula–Hegra region occupies a transitional tectonic position between two distinct seismic provinces of the northwestern Arabian Shield (Al-Arifi et al., 2013; Abdelwahed et al., 2020). To the south-southwest, the Harrat Lunayyir volcanic zone was considered dormant until April–June 2009, when a swarm of over 30,000 earthquakes occurred beneath the field, a 5 km fissure opened at the surface, and a M5.4 event in May 2010 caused structural damage in the town of Al-Ays (Al-Arifi et al., 2013). To the north, the Tabuk Structural Zone follows NW-trending fault segments representing the northern extension of the Najd Fault System; historically this zone produced a M7.0 earthquake in March 1068 CE, with intensities of VII–IX and 20,000 casualties, and a further damaging event of comparable intensity in January 1588 CE along the same structural trend (Al-Arifi et al., 2013; Abdelwahed et al., 2020). These two provinces frame a site that is not seismically isolated: Hegra lies within reach of both a recently reactivated volcanic field to the south and a historically active fault belt to the north. Probabilistic seismic hazard assessments for northwestern Saudi Arabia (Sokolov et al., 2017; Al-Arifi et al., 2013) place peak ground accelerations in this region at approximately 0.05–0.12 g for 475-year return periods and 0.10–0.20 g for 2475-year return periods.

The Quweira quartzitic sandstone, composed of Cambrian litharenite to quartzarenite with predominantly fluvial and tidal-influenced facies, hosts all rock-hewn tombs. Grain size, colour, and cementation vary significantly, leading to diverse mechanical behaviours (Wahbi, 2014). Petrographic analysis (Saleh et al., 2021) identifies ~95% quartz (confirmed by XRD in Section 3.1), with silica and iron-oxide cements, kaolinite patches, and occasional salt crystals in pores. Variability in cementation, from weakly bonded kaolinite-rich zones to tightly silica-cemented beds, controls the bimodal mechanical quality distribution. NE-, NW-, and EW-trending joints control erosion, producing massifs with rounded peaks, pillars, and ridges; alveolar weathering is widespread (Young and Young, 2012; Paradise, 2013; Beni et al., 2023). A silty-clayey layer 1–2 m below the wadi plain surface hosts a shallow groundwater system (Jaussen and Savignac, 1914), currently at significantly lower levels than historical observations (Nehmé, 2015; Courbon, 2008) and water well depths, which defines the base hydrological conditions for capillary rise.

3. Climatic setting

Climate data were derived from a Meteoblue dataset for the Al-'Ula airport station (1985–2022), supplemented by published summaries (Weatherspark, 2020; Al-Faqeer, 2009; Vincent, 2008). The province is hyper-arid, with long hot summers and mild winters. Annual mean air temperature (2 m above ground) is 23.9 °C (σ = 9.5 °C), absolute range − 7.7 °C to 46.6 °C, interquartile range 17.5–30.7 °C (Fig. 3). Average maximum daily temperatures are ~35 °C in May–September and ~ 24 °C in December–February; average minimum daily temperatures are ~21 °C and ~ 5 °C for the same periods. A warming trend of approximately +0.3 °C per decade is visible in the 1979–2021 long-term record.

Annual average relative humidity ranges from 20% (summer) to 40% (winter), with the dew point routinely crossed on cool winter and spring mornings. Rainfall is sporadic, concentrated from autumn to spring (January most frequent). Mean annual totals range from 29 to 46 mm across sources (Al-Faqeer, 2009; Agriculture Ministry of KSA, 2004; BRGM, 1977; Vincent, 2008), with pronounced inter-annual variability. Near-zero years alternate with years exceeding 80–100 mm with single events reaching 47 mm in 24 h. Recent flash floods in the wadi have reached ~1 m water depth, with road embankments concentrating runoff toward the massif bases.

The temperature at a rock façade surface differs substantially from the air temperature recorded at 2 m above ground in standard shaded conditions. The orientation-dependent rock surface amplitudes (e.g. $\Delta T \approx$ 38–50 °C diurnal range for south-facing façades) constrain the thermal forcing parameters adopted in the fracture mechanics model and can be validated through IR thermography.

4. Methods

The study combines field observations, in situ and laboratory geomechanical characterisation, an analytical fracture mechanics model with probabilistic Monte Carlo simulation, infrared thermographic field surveys, and three-dimensional finite element modelling.

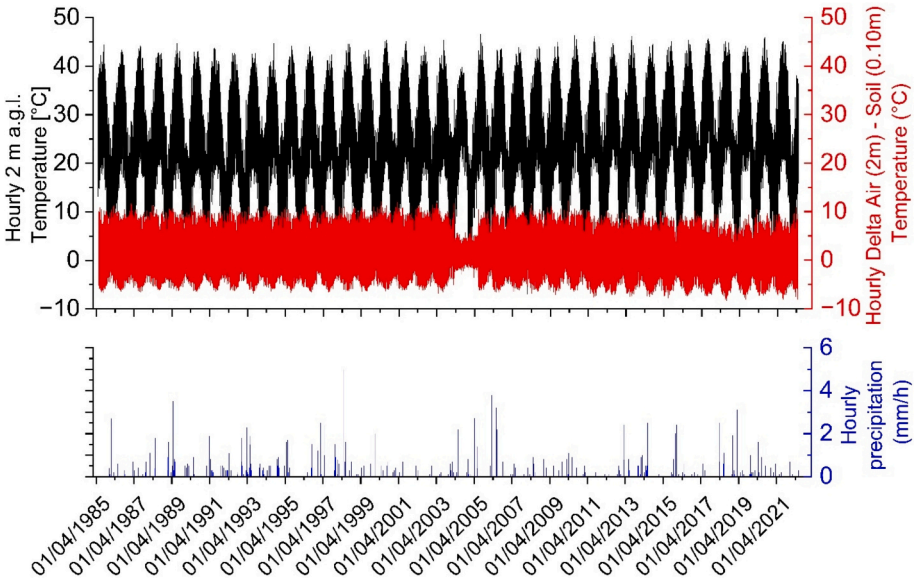

Fig. 3. Meteoblue dataset for the Al-'Ula airport station (1985–2022); hourly air and soil temperatures, and precipitation records.

4.1. Geomechanical testing

Sample availability of Quweira sandstone was limited by heritage conservation constraints; the number collected was considered representative of the main lithological facies even if large variations are observed. The test suite included: uniaxial compressive strength (UCS) and indirect tensile strength (Brazilian) tests under dry and saturated conditions; multistage triaxial tests; slake durability tests; capillarity imbibition tests with simultaneous infrared thermographic monitoring; Richards' plate extractor tests; and Mercury Intrusion Porosimetry (MIP). XRD and grain size analyses were performed on loose surface material and slake durability residues. Additional tests on samples after a complete wetting–drying cycle in the Richards' plate extractor isolated the irreversible component of moisture-induced strength reduction. Multistage triaxial tests used 4–9 successive loading steps per sample at increasing confining pressures, with Mohr–Coulomb envelope fitting.

4.2. Capillary imbibition tests

Capillary imbibition tests (Franzen and Mirwald, 2004) combined continuous gravimetric recording with infrared thermographic monitoring. Cylindrical samples were placed with their base in contact with a constant-level water surface, and sample weight was recorded (0.001 g resolution, 1-min intervals) as the water front rises. A simultaneous IR camera survey visualises wetting front advance through the associated surface temperature change, with the wet zone cooling relative to the dry zone by evaporative heat exchange. Weight gain and wetting front rise both follow a square-root-of-time relationship, and normalising cumulative weight gain by basal area yields the coefficient of capillarity, W_s [g cm^{-2} s$^{-1/2}$].

4.3. Thermal stress and fracture propagation

The onset of large-scale mechanical instability in the Quweira sandstone is evidenced by the formation of tensile cracks (Case 2),



Fig. 4. Façade deterioration by erosion and parallel (a, b, c) and perpendicular (d, e) to façade crack propagation. a) IGN55 tomb façade, b) parallel-to-façade crack (Case 2 propagation in the paper) forming a 4–5 cm thick rock slab; c) side view of an upper 4–5 cm thick slab; d) corner crack (Case 1) at Qasr Al Farid tomb façade (IGN110) close to lateral return face. Stress concentration at the geometric discontinuity drives inward fracture instead of Case 2 spalling. e) vertical tensile cracks (Case 1), perpendicular to façade, with 1.2 to 1.5 m spacing.

typically developing 4–5 cm behind and parallel to the main tomb façade (Fig. 4a,b, c). These fractures are visible where façades are cut at the base or laterally. Tensile cracks perpendicular to the façade are also observed (e.g. at Al Farid tomb, Fig. 4e). Corner cracks (Fig. 4d) represent the Case 1 geometry operating at a stress-concentrated geometric discontinuity. These are generated where biaxial thermal loading and gravitational bending combine to drive a deepening fracture at the façade–rock mass interface, rather than the surface-parallel Case 2 geometry. To understand the propagation of these features, we apply a thermal fracture mechanics model based on the diurnal thermal loading cycles observed at the site. (See Fig. 5.)

4.3.1. Heat conduction and surface forcing

Heat conduction in a semi-infinite half-space under periodic surface forcing gives the steady-state temperature field (**Carslaw and Jaeger, 1959**): $T(x,t) = T_{mean} - A{\cdot}exp(-x/\delta){\cdot}cos(\omega t - x/\delta)$ where x is depth below the façade surface, $A = \Delta T/2$ is the diurnal temperature semi-amplitude at the surface, $\omega = 2\pi/P$ is the angular frequency (P = 86,400 s), $\delta = \sqrt{(D{\cdot}P/\pi)}$ is the thermal skin depth (i.e. thermal penetration depth at which the surface periodic oscillation decays to 1/e), and D [m^2/s] **is the effective thermal diffusivity. The phase convention** $t = 0$ corresponds to midnight (i.e. surface temperature minimum; maximum tensile stress; crack at maximum opening).

The surface temperature amplitude A at a rock façade differs substantially from the air temperature amplitude measured at 2 m above ground. At the latitude of Al-'Ula (~24°N), parameters are assumed for clear skies (atmospheric transmittance, τ ≈ 0.75), dark-coloured rock (absorptivity a ≈ 0.80), and moderate desert wind (combined heat transfer coefficient h ≈ 18 W m^{-2} K^{-1}). Under these conditions, south-facing vertical façades receive near-perpendicular insolation in winter (sun at low southern angle), reaching surface temperatures of 60–65 °C with diurnal deltas of + 30–34 °C above air temperature. In summer, the sun is nearly overhead and a vertical south façade catches only grazing rays, so T_{rock} barely exceeds T_{air} during midday. South-west-facing façades are the most extreme case, peaking at approximately + 44 °C above air temperature in October when afternoon solar loading combines with already-elevated air temperatures. North-facing façades receive essentially no direct winter sun at this latitude and have a mean annual temperature offset of only approximately + 2 °C above air temperature. These orientation-dependent corrections justify the use of ΔT = 42 °C (σ = 10 °C) for south-facing façades in the Monte Carlo simulation, consistent with the IR thermography observations described below, and with published rock-surface temperature excursions at comparable desert sandstone sites (Heinrich, 2008) or steep and sun exposed outcrops (Collins and Stock, 2016).

The Mode I stress intensity factor (K_I), describing thin-skin spalling that generates a crack parallel to the free surface (Atkinson and Meredith, 1987; Anderson, 2005; Eppes and Keanini, 2017), is driven by the maximum thermoelastic stress along the direction of the temperature gradient: $\sigma(a) = E{\cdot}\alpha{\cdot}\Delta T{\cdot}exp(-a/\delta_{eff})$, **where E [Pa] is an effective Young's modulus (with the** $(1-\nu)$ **term either folded into E or omitted assuming negligible lateral constraints at the very surface of a weathered façade) and α [$°C^{-1}$] is the linear thermal expansion coefficient.** The resulting stress intensity factor is:

$$K_I(a) = 1.12{\cdot}E{\cdot}\alpha{\cdot}\Delta T{\cdot}exp(-a/\delta_{eff}){\cdot}\sqrt{(\pi{\cdot}a)}\ [MPa{\cdot}m^{0.5}]$$

where a [m] is crack depth from the surface. $K_I(a)$ has a maximum at $a^* = \delta_{eff}/2$. This depth a^*, derived numerically from the stress profile, represents the most probable location for stable crack propagation and eventual spalling. Two geometrically distinct crack models are developed. In Case 1 (inward-deepening crack, Fig. 4d and Fig. 4e), the tracked variable is depth a(t) and K_I is self-limiting past a^*. In Case 2 (lateral surface-parallel crack, Fig. 4a, b and c), the crack plane is fixed at depth a^*, the thermal stress at the crack plane is constant: $\sigma^* = E{\cdot}\alpha{\cdot}\Delta T{\cdot}exp(-a^*/\delta_{eff}) = E{\cdot}\alpha{\cdot}\Delta T{\cdot}exp(-0.5)$, and the SIF at the advancing crack front (height h) is:

$$K_I(h) = 1.12{\cdot}\sigma^*{\cdot}\sqrt{(\pi{\cdot}h)}$$

monotonically increasing with h (i.e. no maximum). Because the crack depth does not change as the crack grows laterally, the driving stress σ^* remains constant and only the geometric factor $\sqrt{(\pi{\cdot}h)}$ increases. There is no competing exponential decay. The crack therefore accelerates as it grows, with a runaway mechanism absent from Case 1. Subcritical and fatigue crack growth in both cases follows the Paris–Erdogan fatigue law (Charles, 1958; **Paris and Erdogan, 1963**; **Tada et al., 2000**):

$$dh/dt = C{\cdot}K_I(h)^m\ [mm/cycle]$$

where C [mm/cycle] is the Paris coefficient (crack growth rate at unit SIF), and m [−] is the Paris exponent and $K_I(h)$ is evaluated at the current crack height. Slab stability after full debonding ($h = H_{façade}$ is

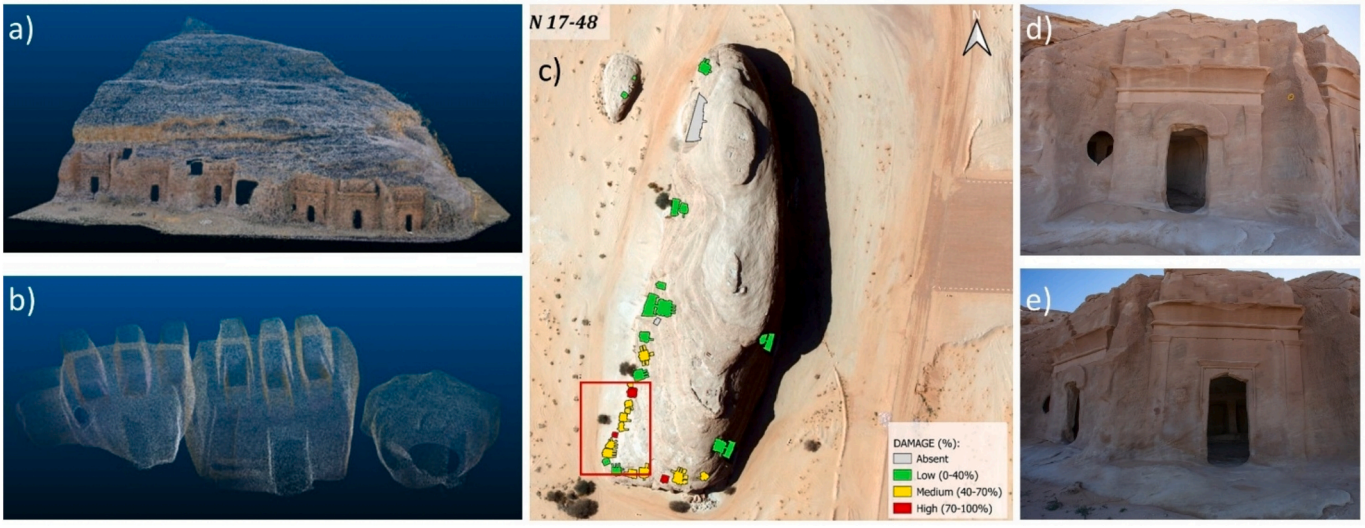

Fig. 5. Qasr al-Bint tomb (IGN29–34), a) and b) point clouds for the inner and outer FEM construction, c) position within the jabal, d) and e) tombs IGN32 and IGN34.

assessed against gravitational overturning, seismic toppling, with critical acceleration $a_{s_crit} = g{\cdot}a^{*}/H_{façade}$), and hydrostatic water pressure in the open crack, with critical fill height $h_{w,crit} = [3{\cdot}(\rho_{rock}/\rho_{water}){\cdot}a^{*2}{\cdot}H_{façade}]^{1/3}$.

4.4. Monte carlo probabilistic simulation

The Paris coefficient C is treated as a log-normal random variable (median $C_0 = 5 \times 10^{-5}$ mm/cycle, log-standard deviation $\sigma_{ln} = 0.5$) to represent natural variability in rock fatigue behaviour. Annual diurnal temperature amplitude ΔT is drawn from a normal distribution calibrated to local climate statistics (μ = 42 °C, σ = 10 °C for south-facing façades; μ = 22 °C, σ = 5 °C for north-facing). Fracture toughness $K_{IC} = 1.5MPa{\cdot}m^{0.5}$ (dry intact) is fixed per realisation and $\boldsymbol{N} = 15{,}000$ Monte Carlo realisations are run over a $\boldsymbol{T} = 2000$-year horizon (i.e. mean tomb life). Each realisation tracks $h_{crack}(t)$ through Phase A (subcritical fatigue growth, $h_0 = 5\ mm \rightarrow h_{brittle}$), Phase B (brittle jump when $K_I(h) \geq K_{IC}$ in any given year), and Phase C (waiting time for slab detachment). Phase C models two independent Bernoulli triggers per year: seismic (annual probability P_{seis}, calibrated to local Arabian Platform hazard at $\boldsymbol{a_{s,crit} = 0.8\%g}$; Sokolov et al., **2017**), and hydrological (annual maximum water fill h_w drawn from a log-normal distribution). **From the ensemble, we computed survival curves, brittle jump year distributions, and T_{50} values for three distinct moisture scenarios:** Dry (μ = 20 mm σ = 25 mm), Base (condensation, μ = 35 mm σ = 50 mm), and Wet (active capillary rise and runoff, μ = 70 mm σ = 100 mm). Sensitivity analysis perturbs ± 20% one-at-a-time six dry mechanical and thermal parameters ($E, K_{IC}, \Delta T, C, \delta_{eff}, \alpha$) and three water-related parameters ($K_{IC,wet}$, C_{eff} multiplier, P_{water}). Water effects on K_{IC} (Noël et al., **2021**) and the Paris coefficient C are treated as multiplicative modifiers with ranges informed by stress corrosion data for quartz and silicate rocks (Atkinson, **1984**; Brantut et al., **2013**; Nara et al., **2011, 2012, 2014**).

4.5. Infrared thermography

At tomb IGN55 (numbering according to Nehmé, 2015) field infrared thermal surveys were carried out on 9 March 2024 using a Bosch thermal camera with emissivity set to ε = 0.67, consistent with values for medium-porosity arkosic sandstone (Salisbury and D'Aria, 1992). Images were acquired at two thermally diagnostic times: 06:00 (nocturnal minimum, maximum thermal contrast) and 16:00 (post-insolation peak, polarity reversal test). The reference temperature T_p was read from an adjacent unaffected surface at each acquisition time. At 06:00, zones of anomalously low surface temperature relative to the surrounding intact rock face indicate thermally decoupled slabs. This is the case of thin laminae or slabs separated from the rock mass by an open crack and having insufficient thermal mass to retain heat from the previous solar day. The spatial boundaries of these cold zones map the lateral extent of the crack, providing an estimate of h_{crack}. The temperature contrast between the cold zone and the intact rock provides an independent check on the calibrated effective diffusivity D_{eff}.

4.6. Finite element modelling

Finite element modelling was carried out using MIDAS FEA NX. Two independent models were developed, addressing complementary aspects of tomb stability and thermal behaviour at different geometric and temporal scales. Two 3D models were constructed to reproduce a geometrically simplified tomb, providing a controlled reference configuration for parametric analysis, and the actual geometry of Qasr al-Bint, capturing the spatial complexity of the necropolis group. Model geometry for the real tomb was derived from terrestrial laser scanner point clouds, processed in *CloudCompare*™ and *Geomagic*™.

Both models were discretised using ten-node tetrahedral elements which allowed us to capture the complex geometry of the rock-cut cavities. The simplified model comprises 265,455 elements and 194,056 nodes; the real-geometry model 3,272,775 elements and 378,192 nodes (Fig. 6). The rock mass was modelled as homogeneous, isotropic, and elasto-plastic with a Mohr–Coulomb failure criterion. Mechanical and thermal properties were determined from the laboratory tests and are summarised in Table 1.

To assess the influence of moisture content on behaviour, cohesion was varied parametrically according to estimated degree of saturation (from 350 kPa at full saturation to 175 kPa at 50% saturation), while friction angle and elastic parameters were kept constant. The base of the models is fully restrained in all three translational directions; lateral faces are constrained perpendicular to each face, leaving in-plane deformation free; the top surface is unconstrained. The simplified model was stratified according to the volumetric water content in three main layers, reaching 1 m, 3 m and 5 m above the tomb base (Fig. 6) and with 50%, 80% and 90% of the dry cohesion value, respectively.

Two analysis types were applied to both 3D models, each tested under uniform cohesion (dry–intact state) and under layered saturation-dependent cohesion (field condition). A transient thermal analysis was used to compute the temperature field and induced stress state at each hour over the 30-day monitoring period. For thermal analyses, temperature boundary conditions were applied to external rock surfaces and internal cavity walls based on hourly field measurements over a 30-day monitoring period at Hegra; the recorded daily differential between external and internal surfaces ranges from 7.2 °C to 18 °C. Base and lateral boundaries were treated as thermally insulating. Model validity was assessed through three independent checks. First, all mechanical and thermal parameters reproduce laboratory-measured values (Table 1), ensuring that yielding initiates at stress ratios consistent with measured strength. Second, the simplified geometry model reproduces analytically known solutions for cavity stability in elastic media under gravity loading, providing a mesh resolution and solver convergence benchmark. Third, the transient thermal analysis reproduces the field-measured external–internal surface temperature differential of 7.2–18 °C at the monitored points, validating thermal boundary conditions and conductivity assignments independently of the mechanical analysis. Full structural validation against measured displacements is not possible at present, since no instrumented monitoring is installed at the site.

Then, a stability analysis was performed by the Strength Reduction Method (SRM), in which cohesion and friction coefficient (tan ϕ) are progressively reduced until numerical non-convergence, identifying the global safety factor and failure mechanism without prior geometric assumptions.

5. Results

5.1. Geomechanical characterisation

5.1.1. Mineralogical composition and grain size

The mineralogical composition of the Quweira sandstone is characterised by a high degree of textural and mineralogical maturity, dominated by quartz. Saleh et al. (2021) on the Qasr Al-Farid tomb identified monocrystalline quartz (sub-angular to rounded) with subordinate polycrystalline grains and sedimentary rock fragments. Their petrographic analysis highlighted the presence of iron-oxide coatings and trace micas (muscovite and biotite) acting as grain binders, alongside localised kaolinite patches within the pore spaces. Our XRD analysis confirms the siliceous nature but provides a more granular quantification of the matrix. Quartz (SiO_2) remains the primary constituent at approximately 95%, while the remaining ~5% consists of a clay fraction dominated by nacrite ($Al_2(Si_2O_5)(OH)_4$) with subordinate chlorite. This mineralogical assembly has mechanical implications for the durability

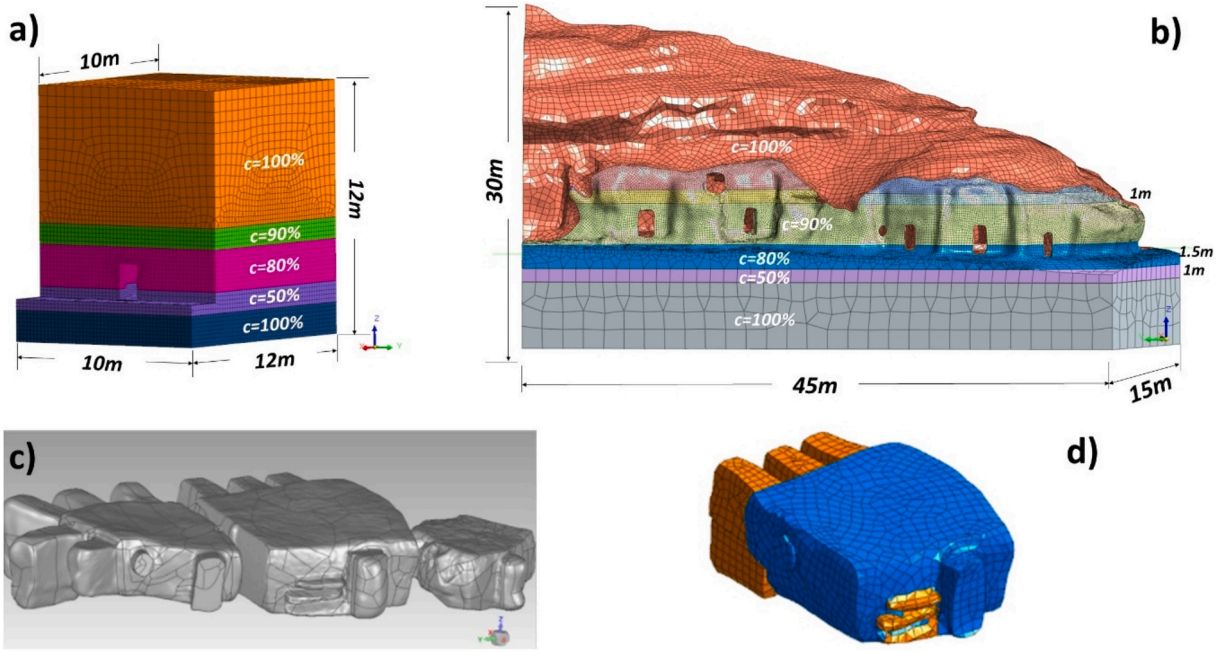

Fig. 6. Finite element models of a) simplified tomb geometry and b) Qasr al-Bint (IGN 29 to IGN34). Both models show the internal subdivision for wet conditions in layers with different cohesion (in percentage with respect to dry cohesion). c) and) surface of the inner chambers and loculi.

Table 1
FEM material parameters for the Quweira Sandstone. Parameters are consistent with laboratory characterisation. Cohesion values represent water-induced strength reduction calibrated against the measured 20–40% tensile strength loss under saturation.

Parameter	Value	Units
Elastic modulus, E	10	GPa
Poisson's ratio, ν	0.4	–
Unit weight, γ	22.5	kN/m^3
Cohesion, c (100% saturation)	350	kPa
Cohesion, c (90% saturation)	315	kPa
Cohesion, c (80% saturation)	280	kPa
Cohesion, c (50% saturation)	175	kPa
Friction angle, ϕ	39	°
Thermal conductivity, λ	2.5	W m^{-1}°C^{-1}
Specific heat, c_p	800	J kg^{-1}°C^{-1}

of the façade. The prevalence of quartz renders the rock skeleton susceptible to the weakening of Si–O–Si bonds upon contact with water. This provides the molecular framework for stress corrosion crack growth, consistent with the hydrolytic weakening documented by Saleh et al. (2021) as water (i.e. hydrolytic weakening) weathering. Although the clay content is low (~5%), the presence of kaolinite-group minerals (nacrite) introduces a slight swelling susceptibility. The hydration of these minerals during wetting cycles contributes to an irreversible reduction in tensile strength, exacerbating the physical detachment of sandstone laminae.

5.1.2. Grain size distribution and erosive dynamics

Grain size analyses of the loose surface material indicate a predominantly sandy distribution, consistent with the fine to coarse observations reported in literature, but with distinct peaks between 0.1 and 1.0 mm (Fig. 7). While the finer silt and clay fractions are present, the sandy fraction represents the primary medium for aeolian abrasion. The dominance of this grain size suggests that saltation is the primary transport mechanism under moderate wind speeds. This creates a focused zone of physical erosion that coincides spatially with the observed height of capillary rise from the ground. The co-spatial

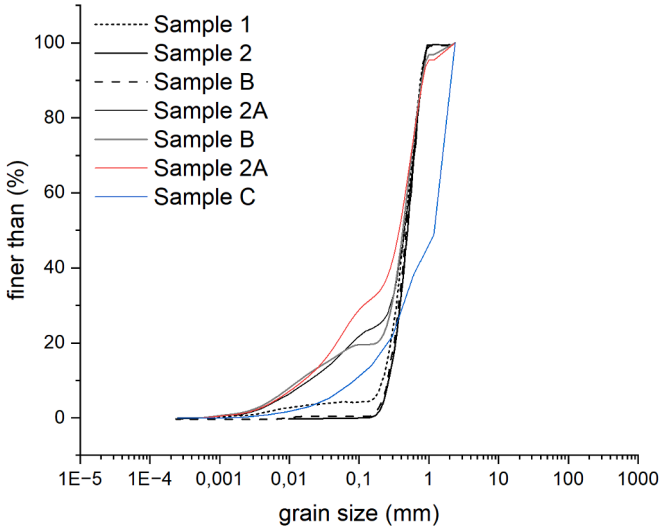

Fig. 7. Grain size curves for the loose sandy samples collected at different sites in the Hegra necropolis.

occurrence of wind-driven abrasion and moisture-related chemical weathering at the façade bases explains the severe deterioration observed in this study and aligns with the bimodal Schmidt hammer distribution reported in subsequent sections.

5.1.3. Capillarity and water retention

Capillarity tests classify the Quweira sandstone as a medium-to-high absorbing rock following Siegesmund and Durrast (2011), with coefficient of capillarity W_s ranging from 0.064 to 0.543 g cm^{-2} s$^{-1/2}$ (Fig. 8, Fig. 9 and Fig. 10). Absorption is rapid in the initial phase and continues slowly thereafter, reflecting a bimodal pore structure with larger pores filling more rapidly than smaller pores. Richards' plate extractor tests (Fig. 10) yield soil water retention curves well fitted by both the Brooks–Corey and van Genuchten models (R^2 = 0.78–0.99). The fitted parameters (Fig. 10) imply a capillary rise under saturated conditions

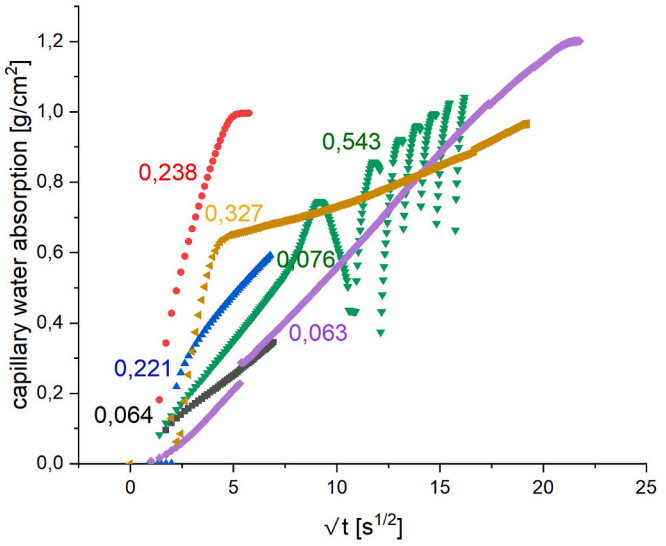

Fig. 8. Capillarity test curves with the values of the coefficient of capillarity for the samples tested by continuous weighting. Coefficient of capillarity is computed considering the initial part of each curve. For one test (in green) the sample was cyclically left draining partially and subsequently rewetted. (For interpretation of the references to colour in this figure legend, the reader is referred to the web version of this article.)

ranging from 0.2 to 3.0 m at the sample scale. This range brackets both the 0.3–1.05 m measured adjacent to the pool (Fig. 2) and the 2–2.5 m maximum rise height observed at the tomb façades, where fracture-controlled pathways and reduced evaporative loss on shaded faces allow water to reach greater heights than in the open pool setting. Air-entry suction values (h_b = 4.5–405*cm*) span over two orders of magnitude. This reflects the wide pore-size distribution implicit in the W_s range and the presence of layering with coarse and finer layers in contact. Finer-pored, weakly cemented samples retain water to higher suctions and support greater capillary rise, controlling which parts of the façade base remain persistently wet between rainfall events. At the same time coarser layers act as preferential drainage paths.

5.1.4. Compressive and tensile strength

Laboratory UCS tests yield 6–22 MPa under dry conditions with no clear saturation effect detectable from the limited sample set (Fig. 11 and Fig. 12). The UCS values higher than 17 MPa correspond to silica-cemented facies. This bimodality reflects at least two distinct mechanical quality domains controlled by cementation degree and weathering state, consistent with the XRD evidence of variable kaolinite-rich versus silica-cemented zones. Brazilian tensile tests show dry values of approximately 1.5–4.0 MPa, with a clear decreasing trend in both compressive and tensile strength with increasing porosity (Fig. 12). P-wave velocity decreases from 3.5 km/s to 1.5 km/s across the porosity range 11.1–21.8% (Gallego et al., 2023).

The most significant moisture effect is on tensile strength. Saturated samples show a consistent reduction of 20–40% relative to dry values, attributable to reduced inter-particle cohesion, softening of kaolinite cement, clay swelling, and reduction of the surface energy of pre-existing microcracks. The latter lowers the energy barrier for Mode I crack propagation. A further irreversible strength decrease is observed in samples subjected to a complete wetting–drying cycle in the Richards' plate extractor (Fig. 10). This implies that cumulative cyclic hydration and desiccation, not peak saturation alone, is the operative degradation mechanism. Salt crystallisation within pores during drying cycles may generate additional microcrack damage, though localised pore-filling by salt can also stiffen the rock. Compressive strength shows markedly less moisture sensitivity, suggesting that the governing failure mode at these façades is tensile, and therefore consistent with spalling, exfoliation, and crack opening under thermoelastic tension (Ruedrich et al., 2011). Nevertheless, the limited number of UCS specimens cannot capture the variability of sandstone lithofacies. The wide mechanical parameter ranges reported here therefore reflect the lithological heterogeneity within the Quweira Formation, confirmed by the bimodal distribution of 710 Schmidt hammer measurements. This heterogeneity motivates the adopted probabilistic modelling approach, with Monte Carlo parameter ranges bracketing the observed variability, rather than using a single mean value.

5.1.5. Slake durability

Over four wetting–drying cycles with weak mechanical agitation, samples A and C lost 15–29% of their mass, while sample B was completely disaggregated after three cycles. This full range of responses, from moderate mass loss to complete disintegration within the same formation, mirrors the bimodal UCS distribution. Furthermore, it confirms that the mechanical quality contrast between cementation domains persists through the rock bulk. The result constrains the upper bound of the Paris coefficient C_{eff} for the wettest scenarios. A rock that disaggregates within four wetting–drying cycles cannot sustain the slow

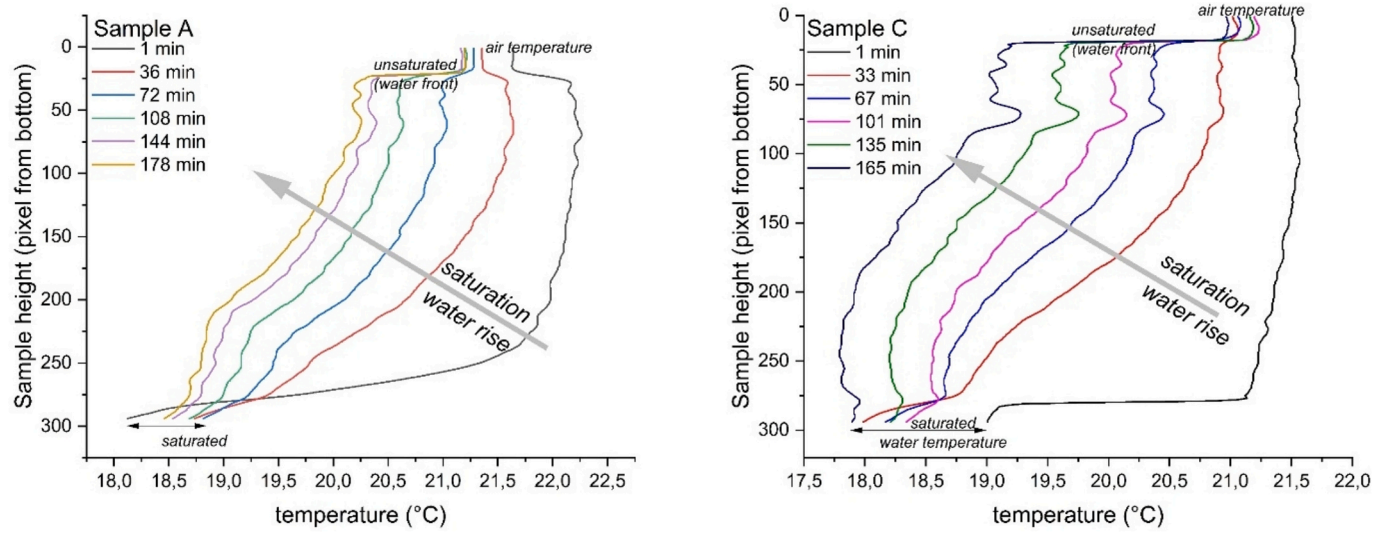

Fig. 9. Profiles of capillary water rise as from two thermographic analyses where temperature increase is related to the progressive saturation. Bottom temperatures refer to water fed to the sample.

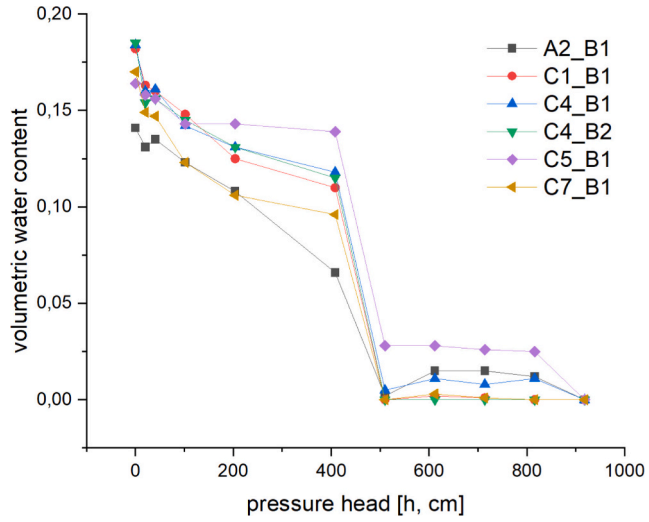

Sample	θ_s	θ_r	α	m	R^2
A2_B1	0.13217 ±0.00519	2.5758e-18 ±0.0175	0.0032375 ±0.00041	0.72327.2 ±0.0869	0.980
C1_B1	0.17891 ±0.00627.2	6.7758e-15 ±0.399	0.022493 ±0.0159	0.1734 ±0.422	0.977
C4_B1	0.1556 ±0.00816	0.008 ±0.0129	0.0024218 ±23.0	0.98869 ±9.08e+03	0.961
C4_B2	0.18401 ±0.00831	1e-10 ±1.01	0.12603 ±0.32	0.09719 ±0.642	0.952
C5_B1	0.1528 ±0.00346	0.026324 ±0.00449	0.0022838 ±0.000138	0.96576 ±0.0286	0.990
C7_B1	0.16912 ±0.00511	1e-10 ±0.24	0.039382 ±0.0245	0.17124 ±0.287	0.987

Fig. 10. *Soil water retention curves determined by the Richards' plate extractor. Data and model fitting parameters for the van Genuchten's model* $\theta(h) = \theta_r + \frac{\theta_s - \theta_r}{[1+(\alpha|h|)^n]^m}$, *are reported in the table.* θs, θr, α, λ *are: saturated water content, residual water content, inverse of bubbling pressure / air-entry value (1/hb), pore size distribution index (=n-1).*

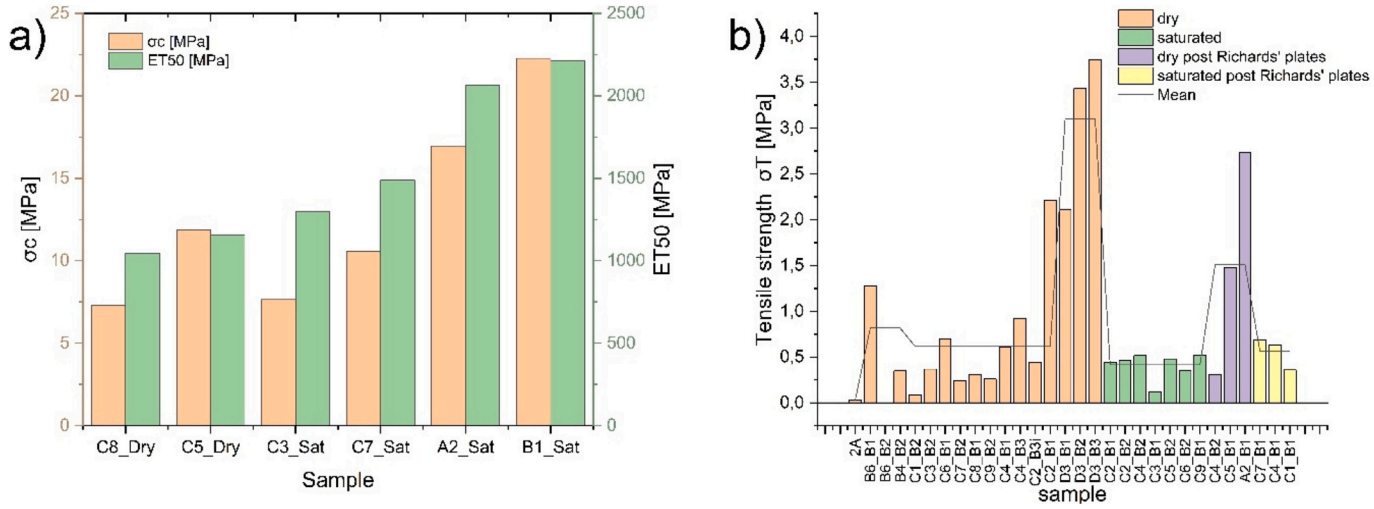

Fig. 11. Histograms showing a) the uniaxial compression test results, and b) the indirect tensile test results for samples tested under dry and saturated conditions. Tensile tests have been performed also on samples previously subjected to a full cycle of saturation-desaturation in a Richards' plate extractor equipment and eventually second saturation.

fatigue crack growth assumed in the base model. On the contrary, it transitions to rapid granular disaggregation, a concurrent but mechanistically distinct damage mode.

5.1.6. Triaxial shear strength

Multistage triaxial tests on four samples (4–9 loading steps each) yield Mohr–Coulomb parameters with friction angle $\phi = 24–49°$ and cohesion c = 3–18.3 MPa. The wide cohesion range reflects variable cementation and is the primary mechanical source of spatial variability in façade stability. It is this range that the FEM strength-reduction scenarios (c = 500 to 200 to 100 kN/m^2) are designed to bracket. A deviation from the linear Mohr–Coulomb envelope at low confinement in one sample suggests non-linear shear behaviour at the low stress levels prevailing at the façade surface, possibly reflecting a bonded-to-frictional failure transition in weakly cemented material.

The material parameters established here, comprising tensile strength, fracture toughness, capillarity, and their moisture dependence, provide the direct input to the fracture mechanics model and the FEM described in the following sections.

5.1.7. Field crack inventory

A photo-based inventory of all the façades identifies crack evidence on 50 facades (53%). 29 façades show Case 1 geometry (inward-deepening cracks, concentrated at upper cornices, architraves, and facade–rock mass corners where biaxial thermal loading applies), 29 show Case 2 geometry (surface-parallel cracks at fixed depth, concentrated at facade bases and wings), and 8 façades show evidence of both geometries. The remaining 44 façades are either in the sub-visual Phase A fatigue stage, or north-facing (predicted stable within the 2000-year simulation window), and affected by other types of fractures (oblique, parallel to layering and laminations, or associated to fractures which extend well within the neighbouring unexcavated rock mass). The spatial distribution of Case 2 cracks is systematically associated with façade zones showing visible alteration and moisture-related surface deterioration, and within the field-measured capillary rise height. Case 1 cracks are concentrated at dry upper cornices and geometric discontinuities unaffected by persistent capillary moisture. The spatial distribution of crack geometries across the necropolis establishes the observational framework quantified through the thermal fracture mechanics model.

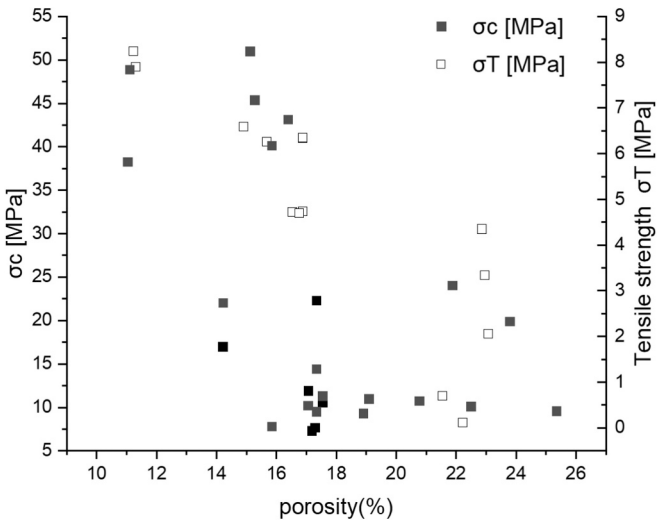

Fig. 12. Compressive and tensile strength values from the laboratory tests plotted against sample porosity.

5.2. Thermal fracture mechanics

5.2.1. Thermal field calibration

Against this observational background, a fracture mechanics model was developed, linking diurnal thermal forcing to the two crack geometries documented in the field. Calibration of the thermal model against the observed crack depth $\boldsymbol{a_{obs} = 40mm}$ yields an effective thermal diffusivity:

$$D_{eff} = 2.33 \times 10^{-7} m^2/s$$

corresponding to a thermal skin depth $\delta_{eff} = 80mm$, ca. 5 times lower than standard unweathered sandstone ($D_{std} = 1.2 \times 10^{-6} m^2/s$, $\delta_{std} = 182mm$). Three physical mechanisms are consistent with this anomalously low value, in detail the tight near-surface cementation reducing inter-granular heat exchange, the desiccation of the outer rock layer increasing its thermal resistance, and the open crack itself acting as a thermal barrier, decoupling the outer slab from the backing rock mass. The practical consequence is that the full diurnal temperature forcing (i.e. surface semi-amplitude of ±21 °C) under mean summer conditions, is concentrated within the outer 80 mm of the façade. This generates steep thermal gradients in the zone where the fracture is observed (Fig. 13a and b). The diurnal cycle drives 365 opening–closing cycles per year providing the basis for the fatigue growth model. The maximum tensile

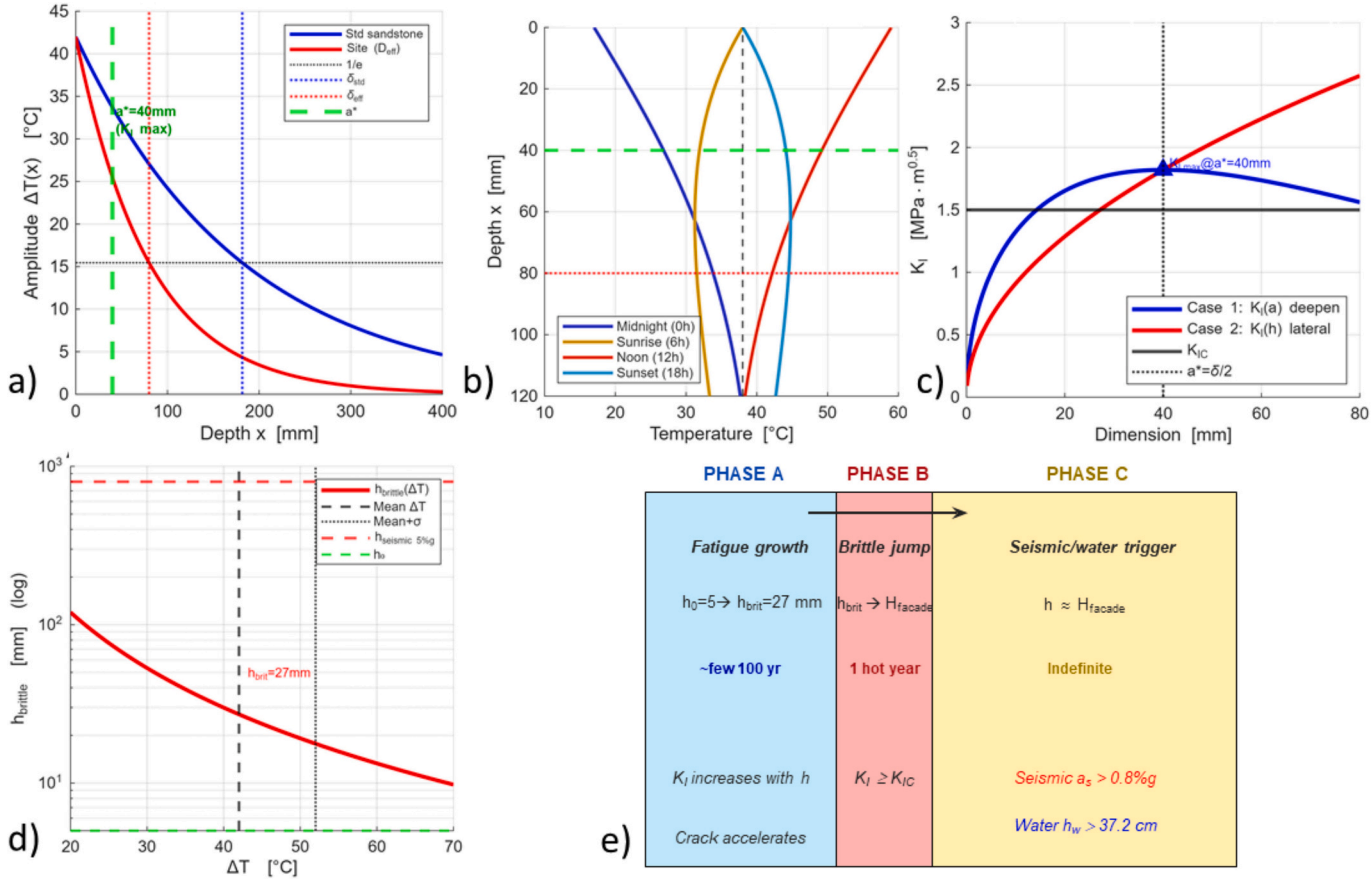

Fig. 13. Thermal lateral spalling model (Case 2). (a) Diurnal thermal amplitude ΔT(x) for standard sandstone ($D_{std} = 1.2 \times 10^{-6}$ m^2/s, blue) and calibrated diffusivity ($D_{eff} = 2.33 \times 10^{-7}$ m^2/s, $\delta_{eff} = 80$ mm, red). At the crack plane depth a* = 40 mm (dashed green), ΔT ≈ 31 °C, produces a thermoelastic stress σ* = 4.58 MPa (E = 20 GPa, α = 9×10^{-6}°C^{-1}). (b) Temperature profiles at midnight, sunrise, noon and sunset. Nocturnal inversion at a* = 40 mm (green dashed) reverses stress at crack plane from compressive to tensile, inducing fatigue Mode I. (c) Stress intensity factor K_I versus crack dimension for Case 1 (deepening crack, K_I(a), blue) and Case 2 (lateral crack at fixed depth a*, K_I(h), red). Unlike Case 1, Case 2 increases monotonically with crack height, h; once it reaches $K_{IC} = 1.5$ MPa · m$^{0.5}$, propagation becomes unstable. (d) Brittle-jump threshold $h_{brittle}$ versus annual temperature amplitude ΔT. At mean ΔT = 42 °C (dashed), $h_{brittle} = 27.2$ mm. Hotter years lower this threshold, increasing Phase B probability. (e) Three-phase failure model: Phase A, subcritical fatigue growth ($h_o = 5$ mm to $h_{brittle}$); Phase B, unstable brittle propagation to full façade height; Phase C, waiting for a seismic ($a_s > 0.8$%g) or hydrological ($h_w > 37.2$ cm) trigger. (For interpretation of the references to colour in this figure legend, the reader is referred to the web version of this article.)

stress is at midnight (early morning, surface at T_{min}; crack at maximum opening), and compressive closure at noon or early afternoon.

5.2.2. K_I profiles and the two-case comparison

The stress intensity factor profiles computed at mean site conditions ($E = 20GPa, \alpha = 9 \times 10^{-6}/^{\circ}C, mean\ \Delta T = 42^{\circ}C, \delta_{eff} = 80mm$) are shown in Fig. 13c. For **Case 1**, $K_I(a)$ rises from zero at the surface to a maximum $K_{I_{max}} = 1.82MPa{\cdot}m^{0.5}$ $(i.e. 121\% of\ K_{IC} = 1.5MPa{\cdot}m^{0.5}$, exceeding the fracture toughness threshold) at $a^* = \delta_{eff}/2 = 40$mm, then decays with depth. This shape reflects the competition between the exponentially decaying thermal stress $K_{IC}\sigma(a) = E{\cdot}\alpha{\cdot}\Delta T{\cdot}exp(-a/\delta)$, and the geometrically increasing factor $\sqrt{(\pi a)}$. At shallow depths the geometric factor dominates and K_I grows; past a^* the exponential stress decay wins and K_I falls below K_{IC} at a depth beyond a^*, providing a finite arrest depth absent from Case 2.

For **Case 2** the crack plane is fixed at $a_{obs} = 40mm$, and does not move as the crack grows laterally. For the self-consistent calibration $\delta_{eff} = 80$ mm ($D_{eff} = 2.33 \times 10^{-7}$m2/s, placing $a^* = a_{obs}$), and the thermoelastic stress perpendicular to the crack plane for given ΔT is

$$\sigma^*_{a_obs} = E{\cdot}\alpha{\cdot}\Delta T{\cdot}exp\left(-a^*_{obs}/\delta_{eff}\right) = E{\cdot}\alpha{\cdot}\Delta T{\cdot}exp(-0.5) = 4.58MPa$$

As crack height h increases, the only term that changes is the crack size h itself, through $\sqrt{(\pi h)}$, so $K_I(h) = 1.12{\cdot}\sigma^*{\cdot}\sqrt{(\pi{\cdot}h)}$ increases monotonically without bound. There is no competing decay mechanism and no maximum. The crack accelerates as it grows, making Case 2 a runaway process absent from Case 1. Fig. 13c directly superimposes the two K_I functions to make this contrast explicit. Brittle jump thresholds shift markedly with ΔT, confirming that hot years trigger fracture at smaller crack heights.

The brittle jump threshold is the Phase A-to-Phase B transition,

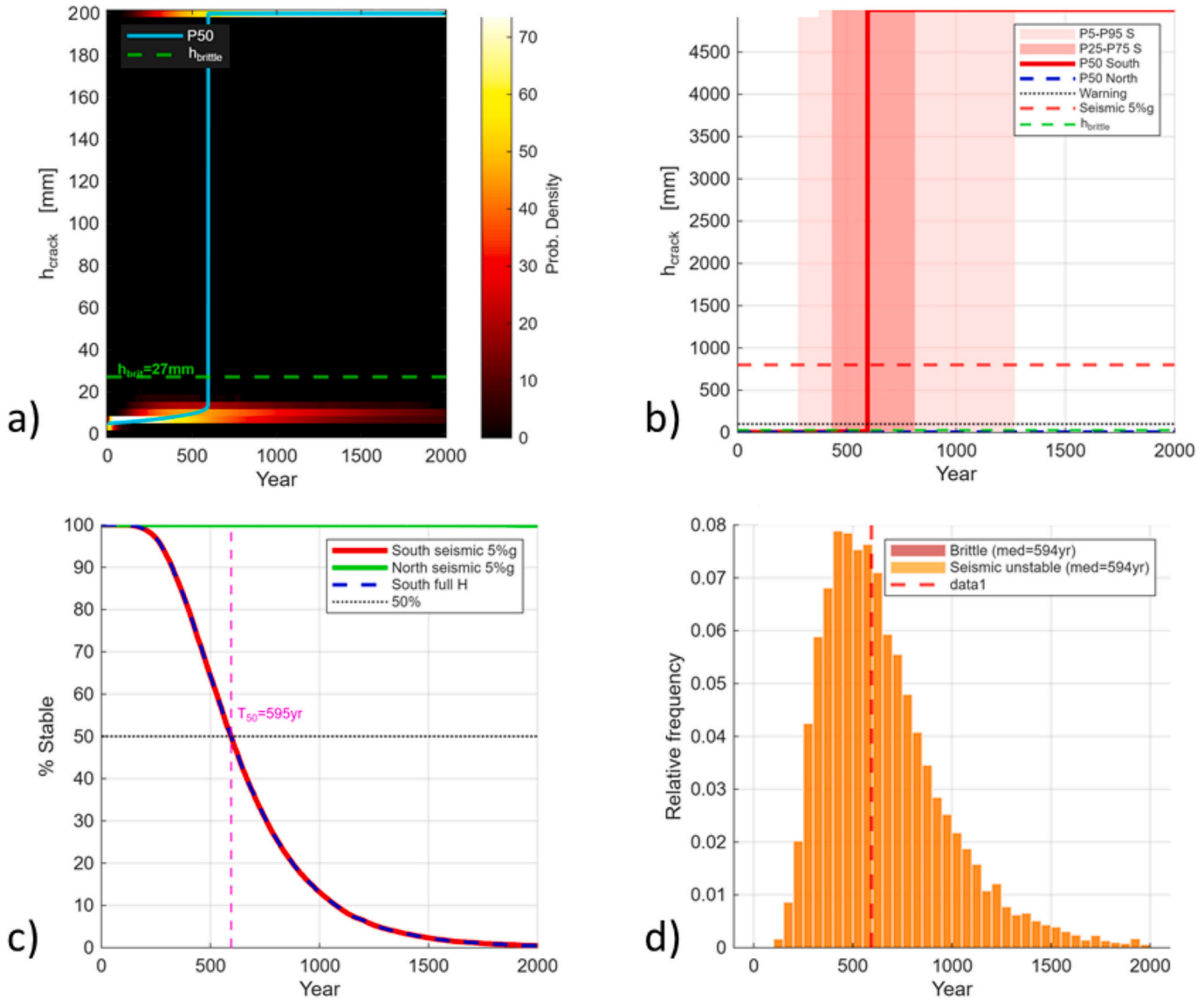

Fig. 14. Monte Carlo simulation of lateral crack growth ($N = 15{,}000$, south-facing façade, 2000-year horizon). (a) Probability density heatmap of $h_{crack}(t)$ during Phase A ($h_{crack} \leq 200$ mm). Cracks advance slowly under daily thermal cycling until it reaching $h_{brittle} = 27.2$ mm (green dashedtriggering a jump to full façade height within an annual cycle (P50 in cyan). (b) Probabilistic envelopes (P5–P95, P25–P75) and median trajectories for south (red) and north (blue) façades. The P50 trajectory for north façades remains near zero; the dashed red line marks the seismic instability threshold $h_{seismic} = 800$ mm at 5%g. (c) Survival curves for south seismic 5%g (red), north seismic 5%g (green), and south full-height (dashed blue). $T_{50} = 615$ yr (dashed magenta). Coincidence of red and blue curves indicates that brittle jump and seismic instability occur simultaneously in Case 2. (d) Distribution of the brittle jump year (median = 603 yr, dashed red). The right skew reflects log-normal variability in the Paris fatigue coefficient (C), with P10 ≈ 300 yr and P90 ≈ 1100 yr. (For interpretation of the references to colour in this figure legend, the reader is referred to the web version of this article.)

corresponding to the crack height at which $K_I(h)$ first reaches K_{IC} and the crack propagates unstably across the full façade height in a single year. At mean $\Delta T = 42$ °C:

$$h_{brittle} = (K_{IC}/(1.12{\cdot}\sigma^{*}))^{2}{\cdot}1000/\pi = 27.2\text{mm}$$

This value is small relative to the façade height (5 m) and is reached after several hundred years of fatigue growth from the initial nucleation height $h_0 = 5$mm.

The IR thermographic survey described below provides an independent field validation of the calibrated effective diffusivity and directly maps the crack geometry used in the Phase C stability analysis.

5.2.3. *Three-phase Monte Carlo results*

The simulation ($N = 15{,}000$, $T = 2000$ yr) produces a well-defined three-phase trajectory for south-facing façades (Fig. 14). During Phase A, the crack grows slowly under subcritical fatigue cycling; median Phase A duration is 603 yr (P10 ≈ 300 yr,P50 ≈ 603 yr,P90 ≈ 1100 yr), with variance dominated by the log-normal spread in C. Fig. 14a shows the probability density concentrated just below $h_{brittle} = 27.2$mm for most of the simulation, confirming that the system spends the majority of its history approaching but not yet crossing the brittle threshold. North-facing façades, with mean $\Delta T = 22$ °C and $\sigma^{*} = 2.4$ *MPa*, never reach $h_{brittle}$ within the 2000-year window and remain 99.4% stable throughout (Fig. 14c). So 14,908 of 15,000 south-facing realisations experience a brittle jump within 2000 years. The remaining 1% correspond to the extreme low-C tail of the Paris coefficient distribution.

Phase B is abrupt and 14,908 out of 15,000 south-facing scenarios (100% to nearest integer) experience a brittle jump within 2000 years, and once $h \geq h_{brittle} = 27.2mm$ the annual probability of the jump

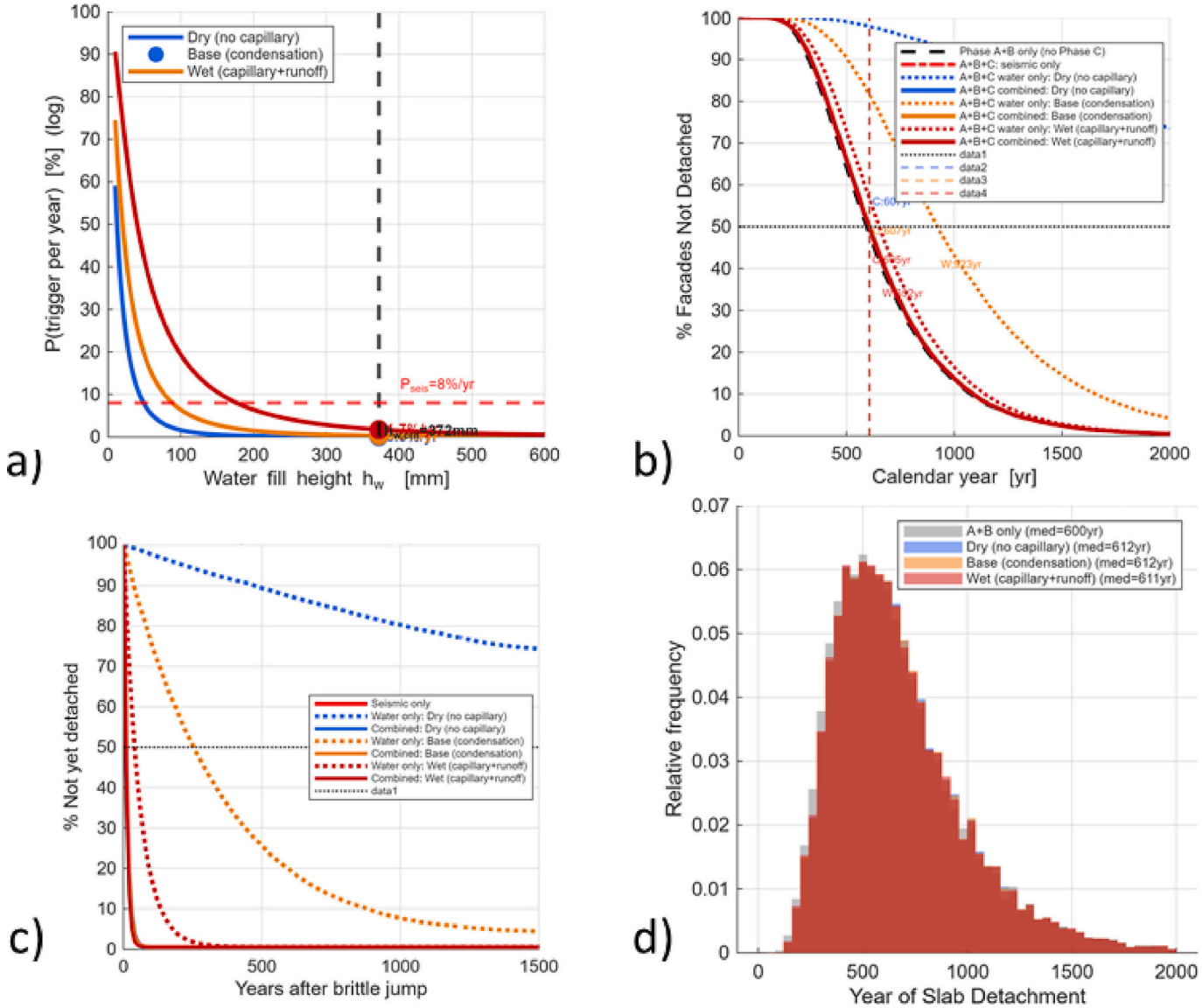

Fig. 15. Phase C trigger analysis: detachment probability under seismic and hydrological loading. (a) Annual water-trigger probability versus crack fill height h_w for dry, base (condensation), and wet (capillary+runoff) scenarios. Critical fill height $h_{w,crit} = 372$ mm (dashed vertical) and seismic reference probability $P_{seis} = 8\%$/yr (dashed red) show water triggers exceed seismic rates only at low fill heights under wet conditions. (b) Combined survival curves (Phases A + B + C). The seismic-dominated curve (dashed-dot red) follows the A + B baseline (dashed black); dry water-only conditions (dotted blue) extend survival beyond 2000 yr. (c) Phase C survival following the moment of brittle jump. The seismic curve (dotted red, $P = 8\%$/yr) reaches 50% in ≈9 yr. The dry water-only curve (dotted blue) shows negligible decline over 1500 yr, confirming seismic dominance. (d) Detachment year histograms (medians 603–615 yr). Overlap indicates that the Phase A + B fatigue governs timing; Phase C contributes <20 yr to the median across all scenarios. (For interpretation of the references to colour in this figure legend, the reader is referred to the web version of this article.)

exceeds 50% (computed from Paris law growth rate under site ΔT distribution). Following the jump the slab spans the full façade height; gravitational stability is preserved (very high safety factor) but the critical seismic acceleration $a_{s_{crit}} = g{\cdot}a^*/H_{facade} = 0.8\%g$ is within the range of minor local seismic events and anthropogenic vibrations. Phase C survival curves (Fig. 15) show that seismic triggering (P = 8%/yr, expected Phase C duration ~12 yr) dominates detachment in dry conditions, while in the wet scenario ($P_{water} \approx 1.73\%/yr$) water and seismic mechanisms compete. Total T_{50} across all combined scenarios ranges from 614 to 615 yr, only marginally longer than the Phase A + B T_{50} because Phase C is short relative to Phase A.

5.2.4. Sensitivity analysis

The tornado diagram (Fig. 16a) ranks parameters by their contribution to $T_{brittle}$ variance. The tornado deterministic base value of 1195 yr is computed at the median C_0 and mean ΔT; the Monte Carlo T_{50} of 603 yr is lower because it integrates over the full log-normal C distribution, for which the mean exceeds the median by a factor exp.($\sigma^2 \ln/2$) ≈ 1.13, and over the ΔT variance. The dominant controls are ΔT (≈38%), thermal expansion coefficient (α ≈ 36%), elastic modulus (E ≈ 35%), C (≈ 30%), K_{IC} (≈22%), and δ_{eff} (≈ 15%) The near-equal sensitivity to ΔT, α, and E reflects the common role of all three in the thermal stress product $E{\cdot}\alpha{\cdot}\Delta T = \sigma^*$. Paris coefficient C (30%) and fracture toughness K_{IC} (22%) follow. The near-equal sensitivity to ΔT, α, and E means that neither material nor climate parameters alone control the risk. A site with lower E but higher surface temperature may carry equivalent or greater risk than one with higher stiffness and moderate temperatures. The effective skin depth δ_{eff} has negligible effect in Case 2 because $exp(-a^*/\delta_{eff}) = exp(-0.5)$ is invariant regardless of δ_{eff}. This is a fundamental difference from Case 1 where δ_{eff} is the third-ranked parameter (Fig. 16a).

Water sensitivity quantifies the double-jeopardy effect. Reducing K_{IC} from 1.5 (dry intact) to 1.0 MPa·m$^{0.5}$ (condensation-wet state; Noël et al., 2021) reduces $T_{brittle}$ from ~1200 yr to ~800 yr; simultaneously increasing C by 4 times (condensation scenario) reduces $T_{brittle}$ to ~80 yr. The combined effect (i.e the physically realistic condensation scenario), is a 15-fold reduction in Phase A duration. **For sites with active capillary rise ($K_{IC_{wet}} \rightarrow 0.5$–$0.7 MPa{\cdot}m^{0.5}, C_{eff} \rightarrow 100$–$500 \times C_{dry}$), Phase A durations collapse from centuries to decades.**

5.2.5. Infrared Thermography

Infrared thermal images of tomb IGN55 (Fig. 17) were acquired at 06:00 and 16:00 on 9 March 2024. The 06:00 image (Fig. 17b), spanning 14.4–29.8 °C (range 15.4 °C), is the primary diagnostic acquisition. Three thermal zones are identifiable. The door frame and intact façade (orange–red, 29.8 °C) represent high-thermal-mass backing rock retaining heat from the previous solar day. The flanking zones on both sides of the door (blue, 14.4 °C) represent the thermally decoupled slab: the thin (~40 mm) lamina separated from the backing rock by the open crack has a thermal time constant $\tau = 4a^2/(\pi^2 \cdot D_{eff}) \approx 0.8$ *hours* and reaches near-ambient temperature within 1–2 h after sunset. The transition zone above the door (green–yellow, ~22 °C) indicates either partial coupling where the crack tapers upward or a second, more recently nucleated lamina still in Phase A. The tomb interior (orange, ~21.7 °C) shows an inverted signal relative to the exterior. The chamber is shielded from nocturnal radiative loss and retains an intermediate temperature unrelated to the spalling mechanism.

The 15.4 °C contrast between intact rock and detached slab constitutes an independent validation of D_{eff}. The thermal model predicts that the intact façade face retains a temperature 14–17 °C above the air-equilibrated slab (40 mm thick with $D_{eff} = 2.33 \times 10^{-7} m^2/s$) at 06:00, consistent with the observed 15.4 °C contrast. The spatial boundary of the blue zone maps the lateral crack extent; its vertical dimension of approximately 1.5–2.0 m on each side of the door provides the h_{crack} estimate used in the Phase C stability analysis. At $h_{crack} = 1.5m$, the critical seismic acceleration is $a_{s,crit} = a_{obs}/h_{crack} = 0.040/1.5 = 2.7\%g$, within the range of minor regional seismic events.

The 16:00 image (Fig. 17c) shows reduced contrast (23.1–30.9 °C, range 7.8 °C) and reversed polarity. The detached slab flanks (yellow–green, ~27.2 °C) are now slightly cooler than the directly irradiated intact façade (red, 30.9 °C), as the slab heats and dissipates faster than the backing rock due to its lower thermal mass. The tomb interior (blue, 23.1 °C) shows the corresponding daytime thermal inversion, protected from direct solar radiation. This polarity reversal between 06:00 and 16:00 is the diagnostic signature of thermal decoupling, and its interpretation against alternative explanations is examined in the Discussion. The 06:00 acquisition time is optimal for crack detection, because maximum contrast coincides with maximum tensile stress, and systematic repeat surveys at 05:00–07:00 can monitor h_{crack} evolution non-invasively.

The building-scale structural context for the spalling mechanism is

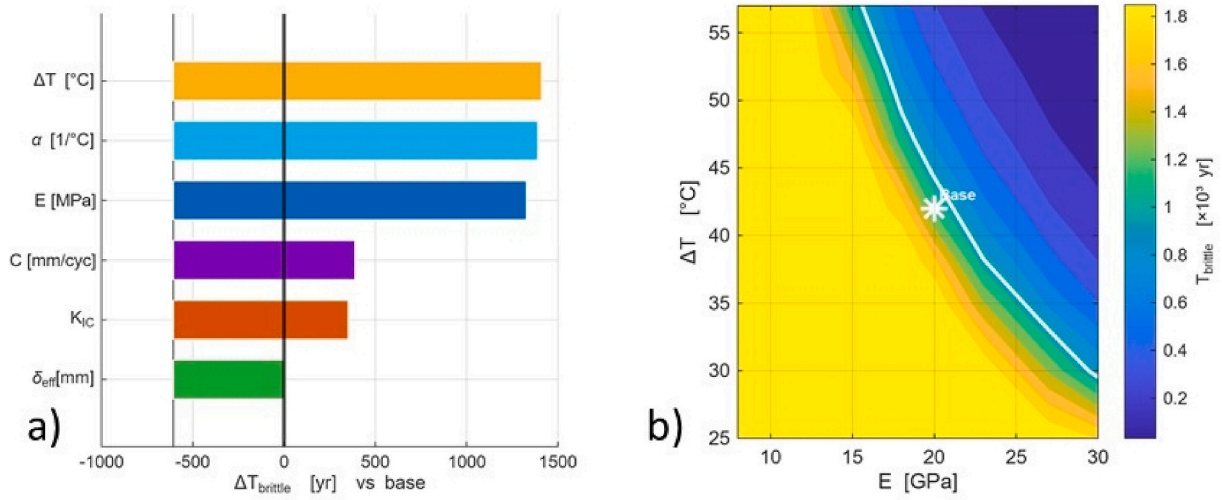

Fig. 16. Sensitivity of Phase A fatigue duration ($T_{brittle}$) to mechanical and thermal parameters. (a) Tornado diagram of $T_{brittle}$ deviation under ±20% perturbations from the base case ($T_{brittle}$ = 1195 yr; E = 20 GPa, K_{IC} = 1.5 MPa·m$^{0.5}$, ΔT = 42 °C, δ_{eff} = 80 mm, C = 5 × 10^{-5} mm/cycle). Thermal amplitude (ΔT) and expansion coefficient (α) are the dominant controls; both influence via the thermoelastic product (E·α·ΔT) raised to the Paris exponent (m = 3.2). (b) Map of $T_{brittle}$ as a function of E and ΔT. The asterisk marks the base scenario; the white contour marks $T_{brittle}$ = 1000 yr. A 6 °C increase in mean ΔT reduces $T_{brittle}$ by ≈40%, regardless of elastic modulus.

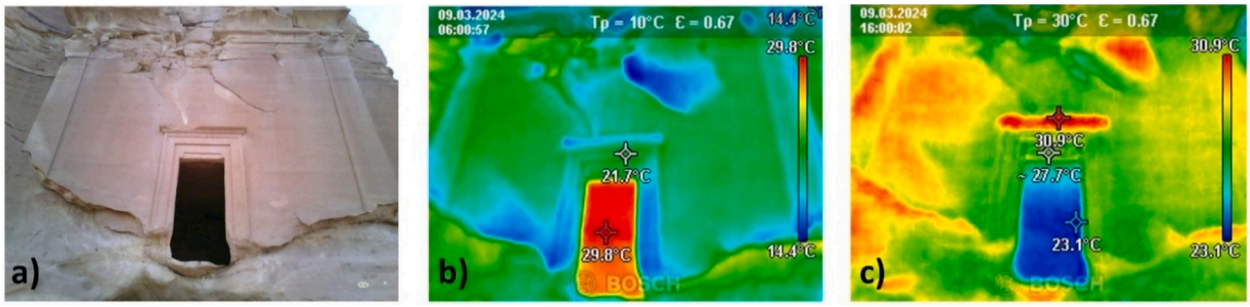

Fig. 17. Infrared thermography for the SSE oriented façade of IGN 55 tomb taken on March 9th, 2024; b) acquisition time 6:00 AM; c) acquisition time 16:00 PM.

addressed in the FEM section that follows, which examines global stability under intact conditions and under the moisture-induced cohesion profiles implied by the capillarity data.

5.3. Finite element modelling

5.3.1. Thermal analysis

The transient thermal analysis on the real Qasr al-Bint geometry reveals a continuously evolving temperature field driven by the daily external–internal differential of 7.2–18 °C (Fig. 18). At midnight (00:00) and sunrise (06:00), the external face is at its daily minimum while the rock mass retains residual heat. This produces tensile stress concentrations at the outer surface and at the pillars between adjacent cavities. By midday (12:00) the thermal gradient reverses and compression dominates the outer surface. The most pronounced deformations occur during the warmest hours and are concentrated at cavity openings and at the pillars, the geometric discontinuities where confinement changes abruptly. The internal tomb chambers show a delayed and attenuated thermal response relative to the exterior, consistent with the thermal inertia of the sandstone quantified by D_{eff}, and with the inverted thermal signature recorded in the IR images. Under thermal loading alone, plasticity is limited to narrow zones immediately around cavity boundaries. The rock mass as a whole remains within the elastic domain. This confirms that thermal stresses at the building scale do not alone drive widespread plastic failure, and that the spalling mechanism operates at a scale (the outer 40–80 mm) that the building-scale FEM does not resolve.

5.3.2. Stability analysis of simplified geometry

Under uniform cohesion of 350 kPa (dry–intact rock), the SRM analysis yields a safety factor FS = 5.44. The failure mechanism is a deep sliding surface developing below and around the cavity, mobilising a large rock volume. Vertical stresses redistribute progressively toward the pillar bases as the reduction factor increases. When cohesion is assigned by saturation layer (350 kPa at full saturation to 175 kPa at 50%), the safety factor drops to FS = 4.51 (17% reduction) and the failure mechanism changes qualitatively. Instead of deep sliding, a plastic hinge forms at the base of the outer pillar, driving overturning of the surface rock volume (Fig. 19). This shift from a deep to a frontal mechanism is attributable to the reduced cohesion of the partially saturated surface layers. This is consistent with the observed pattern of façade loss at Hegra, where thinning and forward collapse of the outer face is the dominant damage mode (Fig. 19). The capillary rise heights of 0.3–1.05 m measured in the field correspond to saturation of the lower

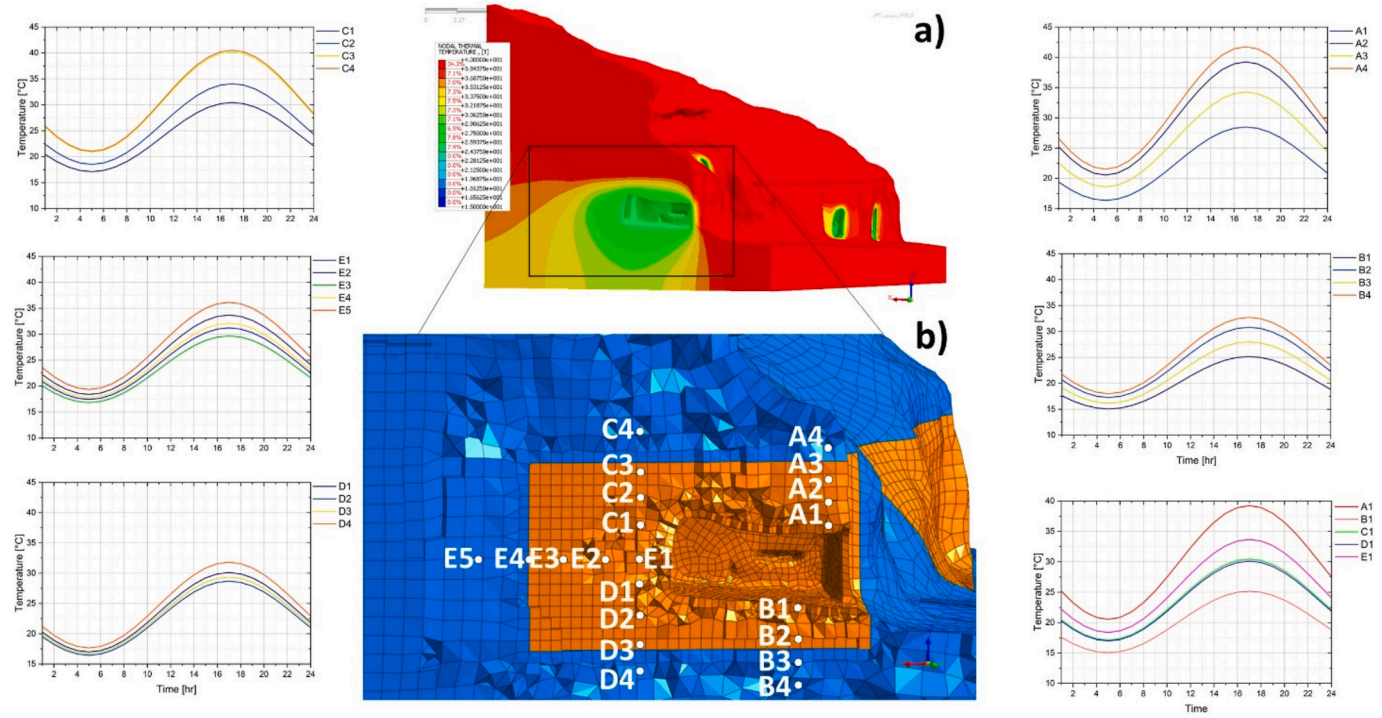

Fig. 18. FEM results for the Qasr al-Bint tombs group (IGN29–34) showing a) the temperature distribution at h 18.00 and b) cross section of the model with some monitored points. Hourly temperature oscillation at different monitored points, at the chamber inner surface and within the rock mass, are reported.

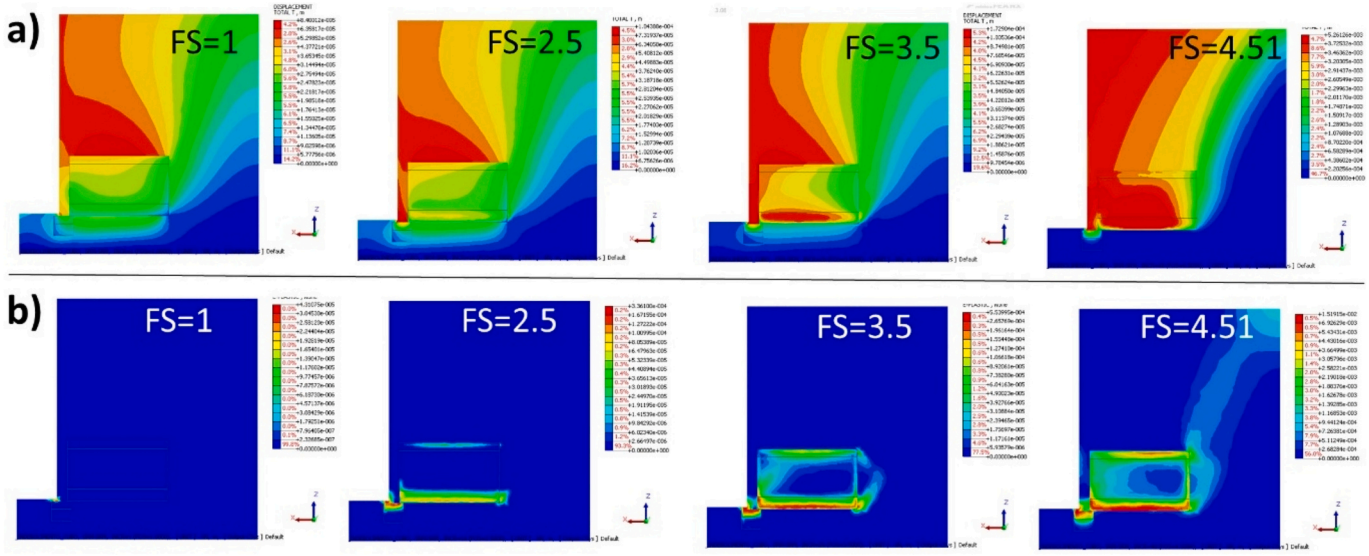

Fig. 19. FEM results for the 3D simplified tomb geometry showing the factor of safety, a) the change in displacement distributions and of b) plastic strain, with SRM properties degradation. The change in the expected type of instability is also evident.

façade zone where the plastic hinge develops, providing a mechanistic link between field hydrology and numerically predicted failure mode.

5.3.3. *Stability analysis of Qasr al-Bint tombs*

The real-geometry model with uniform cohesion does not reach failure within the explored reduction factor range, with FS > 6. The more complex three-dimensional layout of Qasr al-Bint, where the spatial arrangement of pillars and shared walls provides additional confinement, produces substantially higher margins than the simplified geometry (Fig. 20).

Fig. 20a and Fig. 21b illustrate the spatial distribution and the evolution of effective plastic strains computed at specific monitoring points. Both inside and outside the tomb, the effective plastic strains remain negligible during the initial excavation phases (Exc_Tomb, Exc_RetroTomb, and Exc_FrontalTomb), indicating that the rock mass behaves elastically under the as-built excavation conditions. As the Strength Reduction Factor (SRF) is increased beyond FOS = 4.0–4.5, a marked acceleration in plastic strain development is observed at selected monitoring points, signaling the onset of localised yielding within the rock mass. In Fig. 20a, points P1 and P2 exhibit the most pronounced plastic strains, reaching values on the order of 1.5×10^{-3} at the maximum applied SRF. This suggests that the base of the tomb complex represents the most critical zone with respect to stability. In Fig. 20b, point P7 governs the response, accumulating strains of ca. 0.6×10^{-3}, while the remaining points display moderate deformation. The progressive and accelerating nature of the strain–SRF curves provides an indication of the global factor of safety of the system, demonstrating adequate stability margins under the current excavation geometry and rock mass properties.

Plastic zones develop progressively from cavity boundaries inward,

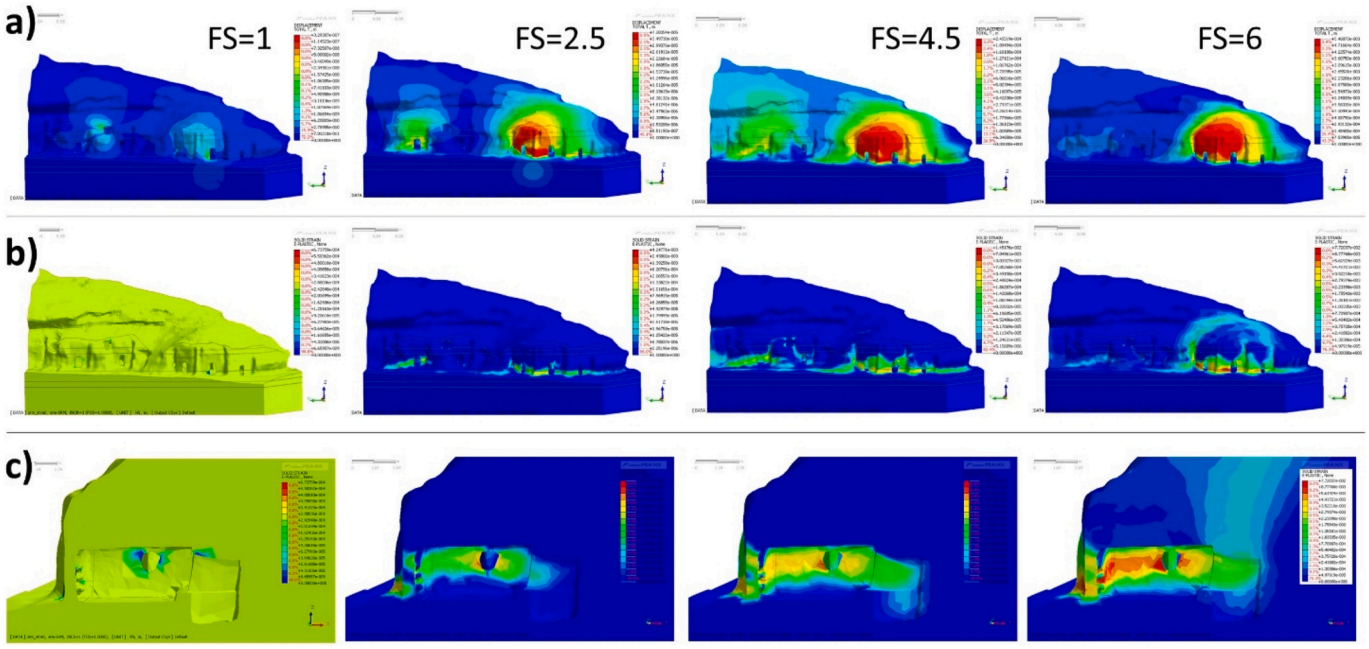

Fig. 20. FEM results for the 3D Qasr al-Bint tomb geometry showing the factor of safety, a) the change in displacement distributions, b) and c) the plastic strain, with SRM properties degradation. The change in the expected type of instability is evident.

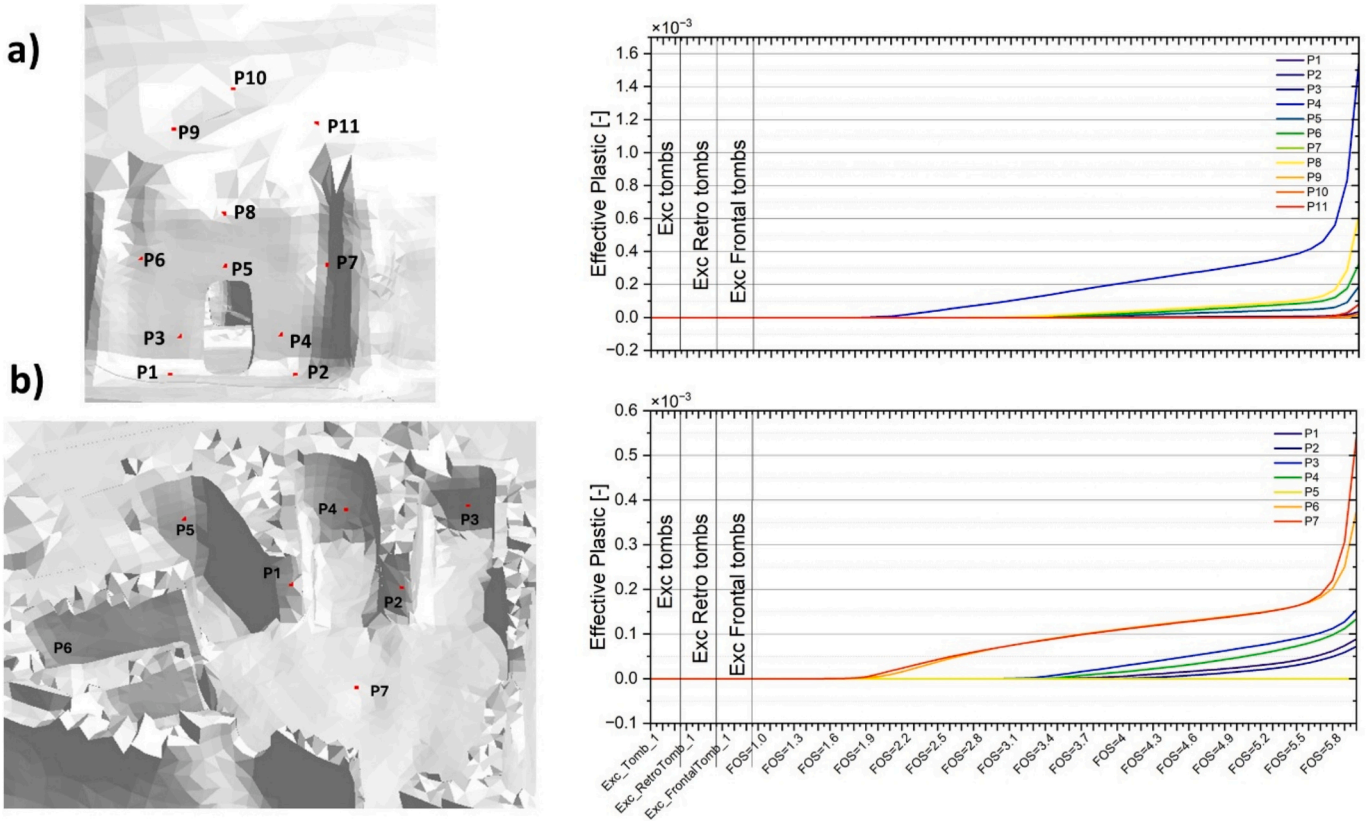

Fig. 21. FEM results for the 3D Qasr al-Bint tomb geometry showing the plastic strain evolution at different monitoring points during progressive SRM properties degradation; a) along the tomb façade, b) within the tomb chambers and loculi. Plastic strain distributions are validated qualitatively against the observed pattern of façade thinning and forward collapse documented across the Hegra necropolis (Fig. 1), and quantitatively through the material parameter calibration in Table 1 and the thermal boundary condition reproduction in Fig. 18.

with a deep sliding mechanism analogous to the simplified homogeneous case. Under saturation-layered cohesion, complete failure is not reached within the explored range, but the failure kinematics change markedly. A plastic hinge develops at the base of the outer pillar and the overlying rock volume (i.e. vault and roof slab) begins to move as a quasi-rigid body. Comparison of displacement histories at three internal monitoring points (vault, pillar, roof slab) between the two configurations confirms qualitatively different structural responses. The layered model shows substantially larger relative displacements between façade elements at equivalent reduction factors. This indicates that moisture-induced cohesion loss selectively destabilises the outer structural elements while the deeper rock mass retains enough strength. The emergence of the plastic hinge mechanism in the layered-cohesion configuration, and its absence in the uniform case, confirms that the spatial distribution of moisture, and not just its mean level, controls the failure mode. This has direct implications for conservation. Interventions that limit capillary rise to the lower façade (e.g. drainage, hydrophobic treatment of the base zone) address the sector where strength reduction drives the most critical failure mechanism. The frontal plastic hinge mechanism emerging under saturation-layered cohesion replicates the dominant observed damage mode at Hegra, namely progressive façade thinning and forward collapse of the outer rock volume, providing independent observational validation of the predicted failure kinematics.

The Discussion integrates these multi-scale results into a unified risk assessment framework and examines their implications for conservation monitoring and intervention.

6. Discussion

The results establish a causal chain from diurnal thermal forcing to probabilistic slab detachment, in which façade orientation, moisture regime, and crack geometry each modify the timeline and failure mode. The following sections examine model calibration against field and literature data, the dominant role of water, the mechanical significance of the observed crack geometry, geometric factors that modify the base-case predictions, and the practical implications for conservation.

6.1. Model calibration and physical basis

6.1.1. Temperature forcing

The parameter of primary importance to the fracture mechanics model is the diurnal temperature amplitude at the rock surface, not the air temperature recorded at 2 m above ground in standard shaded conditions. The orientation-dependent surface amplitudes derived in the Methods give a rock-surface diurnal amplitude of approximately 38–50 °C in summer for south-facing façades, justifying the adopted $\Delta T = 42$ °C ($\sigma = 10$ °C). This is consistent with the IR thermography observations (surface temperature 29.8 °C at 06:00 following a March day) and with published rock-surface temperature excursions at analogous desert sandstone sites (Heinrich, 2008; Eppes et al., 2016). For north-facing façades, the equivalent $\Delta T = 22$ °C produces $\sigma^* = 2.4$ MPa and $h_{brittle} > 800$mm, outside the seismically unstable range, explaining why no north-facing brittle failures are predicted within the 2000-year simulation window. The Monte Carlo simulation adopts present-day climate statistics as a stationary forcing over the 2000-year horizon. Palaeo-climate records for the Arabian Peninsula indicate that the Medieval Warm Period and Little Ice Age produced regional temperature

anomalies of ±0.5–1°C (Markowska et al., 2025). These anomalies fall well within the ±10°C standard deviation adopted for the annual surface temperature amplitude ΔT. Furthermore, palaeo-climate shifts represent changes in mean air temperature rather than in diurnal amplitude. Since the fracture mechanics model is driven by ΔT, their effect on crack growth rates is smaller still. Since ΔT dominates the sensitivity (38% of $T_{brittle}$ variance), and the log-normal spread in C already integrates an effective forcing range wider than these anomalies, non-stationarity would affect the absolute T_{50} value but not the relative ranking of risk factors or the structural conclusions.

6.1.2. Nucleation depth self-consistency

The choice $\delta_{eff} = 80$ mm is not imposed but emerges as the self-consistent calibration condition. With $\delta_{eff} = 80$ mm, the depth of maximum K_I in a deepening crack ($a^* = \delta_{eff}/2$) equals the observed crack plane depth $a_{obs} = 40$mm (Fig. 22). Furthermore, K_I (a_{obs} = 40mm) = $K_{IC} = 1.5$ MPa·$m^{0.5}$ exactly when $\delta_{eff} = 80mm$ (Fig. 22d). These two conditions are consistent with a single calibrated diffusivity validated by the IR thermography. Under Case 2 calibration, $K_{I,max}$ at $a^* = 40$ mm equals 1.82 MPa·$m^{0.5}$, which is 121% of $K_{IC} = 1.5\ MPa{\cdot}m^{0.5}$. Hence, in a deepening-crack (Case 1) scenario, a crack that reaches $a^* = 40$ mm would propagate further because $K_I > K_{IC}$ at that depth, stopping at the outer root of the $K_I(a) = K_{IC}$ curve, at a depth beyond 40 mm. The present Case 2 model treats $a^* = 40$ mm as the pre-existing crack plane depth, and the ΔT threshold for initial nucleation is 35 °C, exceeded in ca. 77% of years under present climate (Fig. 22c), confirming that crack nucleation at this depth is a recurrent rather than a rare event, consistent with the observed persistence of the fracture.

6.2. Comparison with literature

Eppes and Keanini (2017) present a review of mechanical weathering and rock erosion by climate-dependent subcritical cracking. They model a crack deepening perpendicular to the surface, equivalent to our

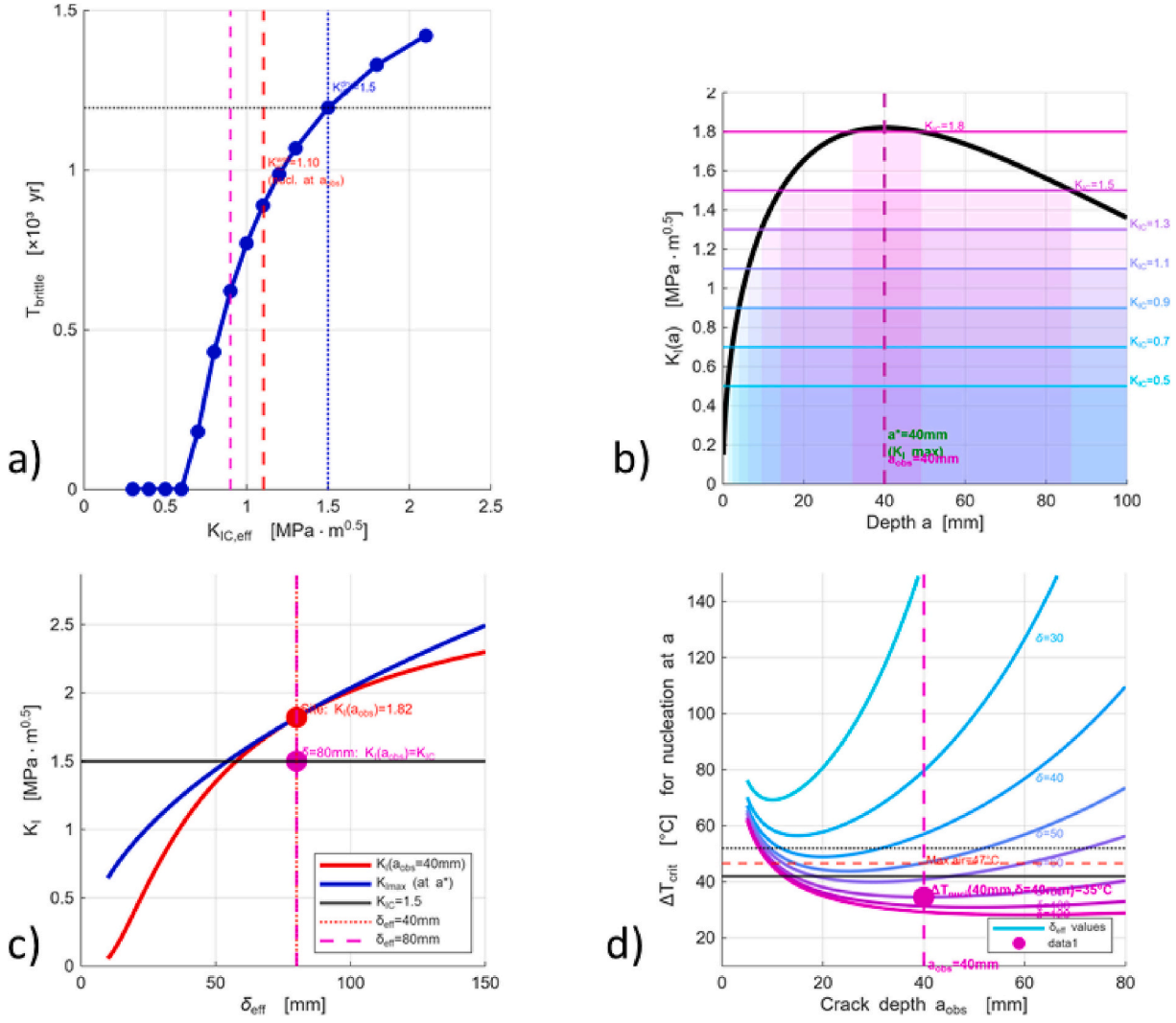

Fig. 22. Model calibration and environmental sensitivity. (a) Phase A duration ($T_{brittle}$) versus effective fracture toughness $K_{IC,eff}$. The dry base value $K_{IC} = 1.5$ MPa·$m^{0.5}$ (blue dotted) gives $T_{brittle} = 1195$ yr. Reducing toughness to $K_{IC,wet} = 1.10$ MPa·$m^{0.5}$ (dashed red, condensation regime) shortens $T_{brittle}$ by a factor of three. Saturation ($K_{IC} < 0.8$ MPa·$m^{0.5}$) collapses failure timescales. (b) Stress intensity factor K_I (a) for a surface-perpendicular crack. Shaded nucleation windows ($K_I \geq K_{IC}$) are shown for six toughness values. Crack depth $a^* = 40$ mm (dashed magenta) coincides with the K_I maximum and falls within the nucleation window for all $K_{IC} \leq 1.82$ MPa·$m^{0.5}$. (c) K_I at observed depth $a_{obs} = 40$ mm (red) and a^* (blue) versus thermal skin depth δ_{eff}. The red curve crosses $K_{IC} = 1.5$ MPa·$m^{0.5}$ at $\delta_{eff} = 80$ mm (magenta dot), meeting the self-consistent calibration condition $\delta_{eff} = 2 \cdot a_{obs}$. (d) Minimum annual temperature amplitude ΔT_{crit} for crack nucleation versus depth a for variable δ_{eff}. At the calibrated site value ($\delta_{eff} = 80$ mm, magenta curves), $\Delta T_{crit} = 35$ °C at $a_{obs} = 40$ mm (filled circle). This threshold is exceeded in 77% of years under present climate (mean $\Delta T = 42$ °C). (For interpretation of the references to colour in this figure legend, the reader is referred to the web version of this article.)

Case 1. This could be the case of the Al Farid tomb, at the corner between the carved façade and the uncarved bulk rock mass behind it (Figure 3Figure 4d). Here, the carved face and the lateral return face are both thermally active, creating **biaxial thermal loading, with** differential expansion and contraction generating a tensile stress oriented **perpendicular to the carved face at the corner junction.** Case 1 geometry identifies daily thermal cycling (rather than extreme one-off temperatures) as the dominant driver, with $K_{I,max}$ at a depth proportional to the thermal skin depth. The present work retains Case 1 as the deepening bound, but it also demonstrates that the lateral geometry (Case 2), consistent with observations, produces a K_I profile monotonically increasing with crack height, with no maximum and no arrest mechanism. This distinction is not addressed by Eppes and Keanini. Furthermore, the present study embeds the fracture mechanics within a Monte Carlo probabilistic framework over a 2000-year horizon, propagating uncertainty in C, ΔT, and K_{IC} into survival curves and risk thresholds. This is motivated by the heritage context, where the relevant question is not whether failure will occur but when, and with what probability, so that inspection intervals can be calibrated.

Collins and Stock (2016) provide a strong observational analogue by documenting rockfall triggering by cyclic thermal stressing of exfoliation fractures. They show that daily temperature cycles drive crack propagation through a Paris-Erdogan fatigue mechanism. The physical mechanism is identical to present Case 2 and similarities include: (i) the surface-parallel crack geometry; (ii) the fatigue rather than static failure mode; (iii) the dominant control of ΔT over T_{max}; and (iv) the autumn peak in events, consistent with higher rock-surface amplitudes when afternoon solar loading coincides with elevated mean temperatures. Differences are rock type (granite vs quartzitic sandstone), crack orientation, scale of detachments, and the heritage context. The crack growth rates implied by the Yosemite observations, with detachments occurring on century timescales, are broadly consistent with the $T_{50} = 615\,yr$ predicted by the present model for a crack growing from $h_0 =$ 5mm to $h_{brittle} = 27.2$mm. The thermal decoupling mechanism at the core of both Case 2 and the Collins & Stock analogue is directly observable at Hegra through infrared thermography, which also enables model validation independently of the fracture mechanics calibration.

6.3. Infrared thermography

6.3.1. Salt efflorescence and the IR polarity

Salt efflorescence, present at the façade base within the capillary rise fringe, was considered as an alternative explanation for the IR thermal anomaly observed at 06:00. Halite ($D \approx 3.6 \times 10^{-6}$m^2/s) and gypsum ($D \approx 0.5 \times 10^{-6}$m^2/s) crusts have diffusivities 15 to 150 times higher than the calibrated rock $D_{eff} = 2.33 \times 10^{-7} m^2/s$. A salt crust would therefore equilibrate more rapidly with the nocturnal air temperature, producing a zone colder than intact rock at 06:00, consistent in sign with the observed anomaly. The polarity reversal observed between 06:00 and 16:00 rules out this interpretation. At 16:00, the detached slab flanks (formerly cold at 06:00) are cooler than the directly irradiated intact façade, whereas a high diffusivity salt crust would heat more rapidly than the rock and would therefore appear warmer. Only a physical air gap (e.g. open crack) produces the observed polarity reversal allowing the slab to cool faster at night, and to heat faster during the day. A compositional anomaly or surface coating cannot change the sign of the thermal contrast, only its magnitude, and the polarity reversal is an unambiguous diagnostic signature of physical thermal decoupling by an open crack.

6.3.2. Infrared thermography monitoring

The 15.4 °C temperature contrast at 06:00 provides three quantitative measurements: (i) independent validation of $D_{eff} = 2.33 \times 10^{-7}$m^2/s. The thermal model predicts a residual temperature excess of 14–17 °C at 06:00 for a 40-mm slab with the calibrated diffusivity, fully consistent with the 15.4 °C contrast; (ii) spatial mapping of h_{crack} (the vertical extent of the cold zone; 1.5–2.0 m at IGN55) estimates the current crack height used in Phase C stability calculations; (iii) identification of secondary debonded zones (i.e. the green-yellow transition zone above the door, ~22 °C at 06:00) reveals either partial coupling where the crack tapers upward or a second, more recently nucleated lamina in Phase A, requiring monitoring attention. Systematic repeat surveys at 05:00–07:00 (maximum thermal contrast) can provide a non-invasive time series of h_{crack} evolution at negligible cost relative to physical inspection, enabling early detection of Phase B approach across the entire necropolis. Direct validation of the fracture mechanics model would require crack-aperture gauges (LVDT or fibre-optic) installed across an open crack, which measure the diurnal opening–closing displacement driving the Paris–Erdogan fatigue law and, through repeated positioning, the lateral advance of the crack. Validation of the continuum FEM predictions is a distinct measurement problem, requiring surface strain gauges or distributed fibre-optic strain sensing on intact rock and pillar faces rather than across a discontinuity. Both require conservation permits at this UNESCO-protected site. A combined programme of pre-dawn IR thermographic surveys and crack-aperture monitoring at tomb IGN55, confirmed in Phase C, would provide the most direct test of the fracture mechanics predictions. For the observed crack at IGN55, already in Phase C, the seismic stability analysis confirms that it deserves immediate structural assessment.

6.4. Water, moisture, and weathering environment

6.4.1. Humidity and stress corrosion

Annual average relative humidity of 20–40% matters for the fatigue model in two distinct respects. First, the dew point is routinely crossed on cool winter and spring mornings. This provides liquid water contact at the crack tip when the nocturnal thermal gradient is at its maximum, and this condensation-tension synergy activates stress corrosion at the moment of greatest mechanical driving force. Second, relative humidity above 60% can activate subcritical crack growth in the Quweira sandstone (95% quartz with silica cement) through adsorbed water films, even without visible condensation, by weakening Si–O–Si bonds at the crack tip through hydrolytic mechanisms of both the matrix and the cementation (Eppes and Keanini, 2017; Atkinson and Meredith, 1987; Nara et al., 2011, 2012). Crack-tip moisture exposure is therefore not limited to discrete precipitation events: on most humid winter mornings the chemical conditions for accelerated fatigue growth are met, as they are when water rises as a consequence of flooding. The XRD-confirmed presence of nacrite (kaolinite-group mineral at ~5%) introduces swelling susceptibility during wetting cycles as another microcrack damage agent, further reducing the effective K_{IC} below values from dry laboratory tests.

The field crack inventory provides spatial confirmation of the moisture–fracture mechanics coupling predicted by the model. Under dry conditions, crack nucleation at a* = 40 mm requires $\Delta T_{crit} > 35^{\circ} C$, exceeded in approximately 77% of years under present climate. Under moist conditions with $K_{IC,wet} \leq 1.5 MPa{\cdot}m^{0.5}$, the nucleation threshold falls below 20 °C, a value exceeded in every year. Case 2 nucleation within the capillary fringe is therefore a near-certain annual event, while nucleation above it remains a probabilistic function of the thermal forcing. The observed spatial segregation, with Case 2 at moist bases and Case 1 at dry upper cornices, represents a fingerprint of moisture-controlled fracture nucleation. This independently validates the double-jeopardy mechanism quantified in the sensitivity analysis.

As a Case 2 crack grows laterally (increasing h), its tip eventually approaches the upper boundary of the observed capillary rise fringe ($h_{cap} = 0.3$–$1.05\,m$), where K_{IC} returns toward the dry value of 1.5] MPa·m$^{0.5}$. A potential arrest mechanism exists if this toughness transition intercepts the crack before it reaches $h_{brittle}$. Under dry conditions $h_{brittle} = 27.2\,mm$ and under wet conditions ca. *6 mm*, both smaller than

the minimum measured capillary rise height, h_{cap}. The crack is always undergoing its brittle jump within the moisture zone, before approaching the dry-strong rock above the fringe. Arrest by the capillary boundary is therefore geometrically precluded for all moisture conditions documented at this site, and the critical crack length is always exceeded before the crack tip exits the wet zone.

Once Phase B has occurred and the crack spans the full facade height, the open fracture itself becomes a preferential moisture pathway. Condensation, dew, and intermittent rainfall collect along the open crack walls, extending effective moisture access above the matrix capillary fringe height. This has two Phase C consequences. First, the effective water fill height h_w in the open crack, which is governed by fracture aperture capillarity and roughness rather than matrix pore capillarity, exceeds the matrix-only estimate and increases the annual hydrological trigger probability. Second, a sustained moisture at the slab perimeter maintains stress corrosion conditions (Si–O–Si hydrolysis) over the full crack height. This progressively reduces residual cohesion at the slab edges. Therefore, the Phase C hydrological trigger probability (Table 2) represents a lower bound for façades with already open cracks. (See Tables 3 and 4.)

6.4.2. Precipitation and the Phase C hydrological model

The episodic, heavy-tailed character of precipitation at Hegra supports the log-normal distribution adopted for the annual maximum water fill height in the Phase C trigger model. Mean annual precipitation ranges from 29 to 46 mm across sources, but the inter-annual variability is extreme, ranging from near-zero years to years exceeding 80–100 mm, with single events delivering 47 mm in 24 h. Flash floods in the local wadis have reached about 1 m water depth with road embankments concentrating runoff against the massif bases. The log-normal distribution captures this behaviour (i.e. low median, long upper tail) without assigning an arbitrary upper bound. For the base-case Dry scenario ($\mu_w = 20\text{mm}, \sigma_w = 25\text{mm}$), the annual probability of filling the crack to the critical height of 372 mm is ca. 0.02%/yr, confirming that gravity-driven hydrostatic failure is negligible under normal hydrological conditions. The Wet scenario ($\mu_w = 70\text{mm}, \sigma_w = 100\text{mm}$, representing active capillary rise plus runoff concentration) gives $P_{water} \approx 1.73\%/\text{yr}$, which begins to be comparable with the seismic trigger probability. Therefore, any modification to site hydrology (e.g altered drainage, vegetation near façade bases, infill of alluvial material) could shift the system into the water-dominated Phase C regime.

6.4.3. Capillary rise, wind abrasion, and thermal fracturing synergy

Three degradation mechanisms converge spatially at the façade base in a positive feedback that could explain the observed severe deterioration. First, capillary rise delivers persistent moisture to this zone, reducing and amplifying the Paris coefficient C relative to dry conditions by the amounts quantified in the sensitivity analysis. At the tomb façades this moist zone extends to 2–2.5 m, so the nucleation-favourable sector covers roughly half the 5 m façade height rather than only the lowest metre. Second, wind abrasion by saltating sand particles K_{IC}operates within the same height range for the modal grain size of 0.1–1.0 mm under moderate to intense desert winds. Third, thermal fatigue crack growth driven by the diurnal cycle operates at its maximum growth rate at the crack plane depth throughout the façade height but is concentrated in this zone by the combined effect of reduced K_{IC} (moisture) and increased C. Wind abrasion removes the weathered outer surface material, maintaining a fresh reactive surface and reducing the effective slab thickness. This in turn lowers the thermal mass and increases the diurnal temperature amplitude available to drive crack growth, while capillary moisture at the crack tip lowers the toughness and amplifies growth rates. Conservation interventions targeting this zone (drainage or hydrophobic treatment of the lower façade) would interrupt capillary rise, reducing crack-tip moisture and wind-driven surface loss. The model predicts a reduction in Phase A duration of about one order of magnitude if $K_{IC,\text{wet}}$ is maintained above 1.1 MPa·m$^{0.5}$.

Table 2
Summary of the probability of failure and T50.

Trigger scenario	P [%/yr]	T_{50} total [yr]
Seismic only (a_s ≥ 0.8%g)	8	~615
Water only — Dry (no capillary)	~0.02	> 2000
Water only — Base (condensation)	~0.28	~908
Water only — Wet (capillary+runoff)	~1.73	~662
Combined — Dry	~8.0	~615
Combined — Base	~8.3	~615
Combined — Wet	~9.7	~614

6.5. Stress effects on weathering and crack propagation

6.5.1. Crack interaction

Brantut et al. (2013) review time-dependent cracking and brittle creep in crustal rocks under sustained stress, noting that crack-tip stress intensity concentrations under static loading can locally exceed the remote applied stress by factors of 2–10. Relevant to the present study is their observation that at moderate crack densities, interaction between sub-parallel cracks can produce mutual shielding reducing the effective K_I at adjacent crack tips and potentially stabilising a crack. At Hegra, multiple sub-parallel lamination cracks at different depths are observed (Fig. 4). If these cracks are sufficiently closely spaced (separation <2–5 crack depths), mutual shielding would reduce the effective K_I at each individual crack tip below the value predicted by the single-crack model, potentially extending the Phase A duration beyond $T_{50} = 615\,yr$. This crack interaction effect is not currently incorporated in the model and represents a conservative bias. The model may overestimate K_I and underestimate $T_{brittle}$ where multiple laminae are present Brantut et al. further note that under wet conditions subcritical crack growth occurs at K_I as low as $0.4 - 0.6{*}K_{IC}$, consistent with the water sensitivity parameterisation adopted here.

A second source of conservative bias in the homogeneous thermo-elastic model is spatial variability in the driving stress itself. The driving stress $\sigma^* = E{\cdot}\alpha{\cdot}\Delta T{\cdot}exp\left(-a^*/\delta_{eff}\right)$ is uniform only if E, α, ΔT, and δ_{eff} are uniform, but in practice all four can vary. A sheltered lower façade zone (e.g. partial sand burial, architectural shadow, or north-facing return) reduces the effective ΔT locally, a softer more porous or a silica-cemented bed reduce or increase E, and a locally wetter zone (capillary rise fringe) changes δ_{eff} through the crack-as-thermal-barrier effect. If σ^* drops over a height interval, for instance, through a persistently shaded or buried zone, $K_I(h)$ at that height may fall below the local K_{IC} and arrest occurs there. In this case the crack front becomes **non-planar.** Case 2 arrest is statistically possible in a heterogeneous rock but requires a specific spatial coincidence between a local K_{IC} maximum and a local σ^* minimum that is large enough to reverse the otherwise monotonically growing K_I. In a uniform façade it never occurs; in the real Quweira sandstone it may delay the brittle jump or produce partial-width crack fronts. This heterogeneity effect acts in the same direction as the Brantut crack-interaction shielding, extending $T_{brittle}$ beyond the homogeneous model prediction. This reinforces the view that the $T_{50} = 615$ yr is a lower bound on Phase A duration for façades with complex rock fabric. It also explains why some tombs show fractures that arrest mid-façade rather than spanning the full width. A direct field test of the heterogeneity effect could be documented, for example, by mapping fracture trace lengths against Schmidt hammer rebound values across individual façade panels.

A first-order quantitative bound can be established by noting that the geometrically relevant quantity for shielding is Δa, representing the centre-to-centre spacing between adjacent parallel crack planes. This is distinct from a^*, the fixed nucleation depth of 40 mm from the façade surface. Shielding is significant when crack planes are spaced less than twice the nucleation depth, $\Delta a < 2a^* = 80\,mm$. Under this condition,

Table 3
Pressure head and relative volumetric content for each Richards' plate extractor tests performed on six Quweira samples.

kPa	0	2	4	10	20	40	50	60	70	80	90
h (cm)	*0*	*20.4*	*40.8*	*102.0*	*204.0*	*408.0*	*510.0*	*612.0*	*714.0*	*816.0*	*918.0*
Sample	Volumetric Water Content										
A2_B1	0.141	0.131	0.135	0.123	0.108	0.066	0.020	0.015	0.015	0.012	0
C1_B1	0.182	0.163	0.160	0.148	0.125	0.110	0	0	0	0	0
C4_B1	0.184	0.160	0.161	0.142	0.131	0.118	0.005	0.011	0.008	0	0
C4_B2	0.185	0.154	0.156	0.145	0.131	0.115	0	0	0	0	0
C5_B1	0.164	0.158	0.156	0.143	0.143	0.139	0.028	0.028	0.026	0.025	0
C7_B1	0.170	0.149	0.147	0.123	0.106	0.096	0	0	0	0	0

overlapping compressive stress lobes reduce the effective K_I at each advancing lateral tip by the factor $(1 - a^*/\Delta a)$ (Kachanov, 1987; Brantut et al., 2013). At the laminae spacings ($\Delta a \approx 30$–50 *mm*, Fig. 4), this gives a KI reduction of 20–50%, extending Tbrittle by a factor of approximately $(1 - a^*/\Delta a)^{(-m)} \approx 1.5$–$3$ for Paris exponent m = 3.2. The $T_{50} = 615$ yr is therefore a conservative lower bound for facades carrying closely spaced parallel laminae.

6.5.2. Gravity versus thermal cyclic stress

Rihosek et al. (2016) demonstrated, through salt weathering experiments, and physical and numerical modelling of Petra monuments, that gravity-induced compressive stress has a negative feedback on weathering. Decay rates follow an exponential decrease with increasing stress magnitude, and unconfined cubes of Umm Ishrin sandstone disintegrated four times faster than cubes loaded to 250–680 kPa. The outer façade surface, the zone of interest in our study, is the portion of a rock-cut monument with the lowest gravity-induced stress, the highest salt crystallisation rate, and the fastest observed recession (0–350 mm/kyr at Petra; Heinrich, 2008). Our work identifies cyclic thermoelastic stress as a second control driving Mode I fatigue crack growth at centimetric depth, following a Paris–Erdogan law and independent of the quasi-static gravity stress field. The two mechanisms are not alternative but spatially co-located amplifiers. Low gravity-induced stress accelerates salt weathering at the surface, while high thermal amplitude drives fatigue crack propagation at depth, and capillary moisture reduces fracture toughness and amplifies the Paris coefficient. Rihosek et al. also observe that sandstone blocks separated from the rock mass by open fractures, as for a detached slab in Phase C of the present model, disintegrate rapidly because the stabilising stress has been lost. This is consistent with the IR thermographic observation at IGN55, where the thermally decoupled slab is in the low-stress condition that Rihosek et al. identify as most vulnerable to accelerated decay. Their call for combining weathering damage assessment with stress modelling and field damage documentation is the framework of the present study. In fact, thermal fracture mechanics quantifies the fatigue damage accumulation, FEM captures the stress redistribution from excavation geometry and moisture-induced cohesion loss, and IR thermographic surveys provide the independent observational validation.

6.6. Geometric controls

6.6.1. Effects of secondary chambers, pillars, and loculi

The FEM results for the Qasr al-Bint tomb group and the collapse of IGN41–42 (Fig. 1a) demonstrate that the spatial arrangement of adjacent tomb chambers, thin inter-tomb pillars, and the network of loculi excavated within the inner façade walls creates stress concentrations absent from a uniform façade. The most pronounced plastic zones develop at pillar bases and at the corners of cavity openings (Fig. 21). At Qasr al-Bint, the spacing between adjacent tomb façades is locally as small as 0.5 m, creating pillars with width-to-height ratios approaching the structural limit for compression arch formation. These pillars concentrate vertical stresses from the overburden and experience the highest thermoelastic stresses during the diurnal cycle, as confirmed by the transient thermal FEM (Fig. 19). The presence of loculi (i.e. niches excavated within the façade) further reduces the effective width of the surface slab between niche edges. Each niche corner acts as a stress concentrator for Mode I opening under the thermoelastic tension generated at the crack plane depth, amplifying the local K_I above the single-crack model prediction, reducing the stress intensity margin against the Phase B threshold. The net effect is that façades bearing complex internal cavity patterns are expected to have shorter Phase A durations than uniform façades of the same rock quality, because the local K_I at the fatigue crack tip is amplified by the stress concentration from the nearest cavity feature. Quantification of this effect would require a coupled fracture-mechanics FEM model at the 10–100 mm scale, which is beyond the scope of the current building-scale FEM but could be addressed by dedicated two-dimensional models for individual pillar cross-sections. The homogeneous isotropic assumption is appropriate at the building scale (1–100 m) at which the FEM operates. Bedding anisotropy and joint sets would reduce the effective strength envelope, and the reported safety factors ($FS = 5.44$ *dry*; $FS = 4.51$ *saturated*) are therefore upper bounds. The frontal plastic hinge failure mechanism, generated at the façade base under saturated conditions, is governed by cohesion reduction in the lower façade layers and is robust to this simplification. The spatial distribution of moisture, not elastic anisotropy, controls the mode shift. The spalling mechanism, at the 40–80 mm depth scale, is not resolved by the building-scale FEM and is addressed by the fracture mechanics model. A coupled multi-scale model incorporating lamination anisotropy remains a valuable future development.

6.6.2. Façade thickness

The thermal skin depth model assumes a semi-infinite half-space. This approximation that becomes inaccurate when the façade thickness W approaches or falls below $2\delta_{eff} = 160mm$. Excluding façades that have already collapsed, the thicknesses of the Hegra façades range from 0.155 m to 2.2 m (mean: 0.5–0.6 m for left- and right-hand façade walls). Measured slab thicknesses, such as at IGN55, are only 40 to 50 mm (behind niches or following cracking). Three distinct thermal regimes can be identified depending on the value of W. For $W > 2\delta_{eff}(> 160mm)$, the semi-infinite assumption holds, and the outer 80 mm experiences the full diurnal amplitude while the inner rock is thermally unaffected. For $\delta_{eff} < W < 2\delta_{eff}(80 - 160mm)$, the thermal wave transmitted through the slab interacts with the inner tomb wall. In this case the effective amplitude driving thermoelastic stress is reduced as the front and back temperature gradients partially cancel. For $W < \delta_{eff}(< 80mm)$, the slab/façade has negligible thermal mass, so it equilibrates almost completely with the ambient air temperature within 1–2 h (large thermal contrast in early morning IR thermography). In fact, the thermal time constant for a 40-mm slab is $\tau = 4a^2/(\pi^2 \cdot D_{eff}) \approx 0.8$ *hours*, and it has two practical consequences for the model. First, once the slab has debonded (Phase C), the driving thermoelastic stress across it drops to zero (i.e. the slab is thermally isolated and no longer loaded by differential expansion). This means that the crack cannot deepen further after Phase B. Second, during Phase A (crack growing laterally at fixed depth), the effective ΔT driving the thermoelastic stress depends on whether the façade above the crack plane is thicker than δ_{eff}.

Table 4
Soil water retention curve parameters for the Brooks and Corey (1964) and Van Genuchten (1980). θs, θr, hb, λ, R2.

	Brooks and Corey					*van Genuchten*				
Sample	θ_s	θ_r	h_b	λ	R^2	θ_s	θ_r	α	m	R^2
A2_B1	0.127.26 ± 0.00467	0.013369 ± 0.00729	374.84 ± 30.3	9.1443 ± 8.67	0.9772	0.13217 ± 0.00519	2.5758e-18 ± 0.0175	0.0032375 ± 0.00041	0.72327.2 ± 0.0869	0.9795
C1_B1	0.1725 ± 0.00791	1e-10 ± 0.729	29.182 ± 21.5	0.16139 ± 0.86	0.9285	0.17891 ± 0.00627.2	6.7758e-15 ± 0.399	0.022493 ± 0.0159	0.1734 ± 0.422	0.9769
C4_B1	0.16833 ± 0.025	1e-10 ± 0.183	95.145 ± 42.2	0.76524 ± 1.77	0.7809	0.1556 ± 0.00816	0.008 ± 0.0129	0.0024218 ± 23.0	0.98869 ± 9.08e+03	0.9611
C4_B2	0.185 ± 0.00903	1e-10 ± 1.03	4.4948 ± 11.4	0.093031 ± 0.681	0.9429	0.18401 ± 0.00831	1e-10 ± 1.01	0.12603 ± 0.32	0.09719 ± 0.642	0.9516
C5_B1	0.1528 ± 0.00346	0.02627.27 ± 0.00457	405.46 ± 3.44	18.48 ± 22.3	0.9904	0.1528 ± 0.00346	0.026324 ± 0.00449	0.0022838 ± 0.000138	0.96576 ± 0.0286	0.9904
C7_B1	0.17 ± 0.0074	1e-10 ± 0.312	11.066 ± 7.38	0.15352 ± 0.386	0.9727.2	0.16912 ± 0.00511	1e-10 ± 0.24	0.039382 ± 0.0245	0.17124 ± 0.287	0.9868

For thick façades ($W \gg \delta_{eff}$), ΔT at depth a* is set by the calibrated 31 °C. For partially thinned façades, near tomb corners or below previous spalling events, the reduced thermal mass amplifies the effective amplitude and may accelerate crack growth, explaining the field observation of concentrated fracture activity at geometric discontinuities (Fig. 4).

Of these three regimes, the Monte Carlo simulation models Regime 1 exclusively ($W > 2\delta_{eff} = 160\ mm$), representing intact thick façades. The field-measured internal–external temperature differential of 7.2–18 °C provides direct validation of this Regime 1 assignment: façades in Regime 2 or Regime 3 would show a progressively smaller differential as the thermal wave couples through the thinning wall, approaching zero in Regime 3 where the wall equilibrates with ambient air. The observed differential confirms that the monitored façades operate in Regime 1 or at the upper boundary of Regime 2, and that the Monte Carlo forcing is physically representative. For Regime 2 façades (partially thinned to 80–160 mm), the reduced driving amplitude extends T_{50} beyond 615 yr and the base-case Monte Carlo overestimates risk for this thinned subset. For Regime 3 façades already in Phase C ($W < \delta_{eff} = 80\ mm$), thermoelastic fatigue effectively ceases and detachment probability depends on the Phase C seismic and hydrological triggers.

6.7. Façade survival rate

6.7.1. T_{50} with 2000-yr survival

Three mechanisms reconcile the modelled $T_{50} = 615\ yr$ with the 2000 year survival of the observable façade population. First, survivorship bias. The 2000-year heritage record is a sample of surviving façades, not a record of all façades. Talus accumulations at the base of tomb groups at Hegra and the recessed surface morphology of numerous façades are evidence of past spalling events. The statistical sample of currently intact façades is biased toward those whose Paris coefficient C is in the low tail of the log-normal distribution (corresponding to the P90 scenarios with $T_{brittle} > 1100yr$ in the model). The $T_{50} = 615\ yr$ is a population median; the observable façades are predominantly those above the median.

Second, cyclic lamination. Each spalling event detaches the outer slab and resets the system at a freshly exposed surface. T_{50} represents the time to the first brittle jump in one spalling cycle, not the total façade lifetime. After a slab detaches, a new nucleation begins at the fresh surface. Multiple spalling cycles over 2000 years are consistent with the model. At $T_{50} = 615\ yr$, 3–4 cycles could have occurred since the Nabataean period, each removing 40–50 mm of façade depth.

Third, the observed crack at IGN55 is already in Phase C, not Phase A. The IR-mapped crack height at this tomb is larger than $h_{brittle}$, meaning the crack has undergone the Phase B brittle jump, and is currently in Phase C, waiting for a seismic or hydrological trigger. The Phase C expected waiting time under dry conditions is ca. 12 years ($a_s > 0.8\%g$, $P_{seis} = 8\%/yr$), meaning this specific slab is at risk of seismic detachment under even a minor earthquake. The observation of an intact but debonded slab is consistent with the model, where the Phase C waiting time is short relative to Phase A, and the slab has not yet encountered a triggering event. This observation motivates urgent monitoring and, if confirmed, stabilisation.

6.7.2. Seismicity context

Against the seismotectonic background, the critical seismic acceleration for Phase C detachment (i.e. $a_{s,crit} = 0.008g$ for a fully debonded 5 m façade) is low relative to the regional probabilistic seismic hazard (PGA 0.05–0.12 g at 475-year return period; Sokolov et al., 2017; Al-Arifi et al., 2013). This threshold is exceeded not only by design-level earthquakes but by minor regional events. The annual probability of 8%/yr used for the seismic Phase C trigger in the Monte Carlo simulation is conservative with respect to tectonic sources alone but physically well-grounded when volcanic and anthropogenic contributions are

included.

The 2000-year continuous survival of Nabataean tomb façades provides an independent geomorphological upper bound on experienced ground motion at Hegra. Slender architectural elements (e.g. engaged columns, cornices, and carved friezes) have survived through the M7.0 event of 1068 CE and the 1588 CE event, both originating from the Tabuk Structural Zone. This survival is consistent with the model for two reasons. First, at 200–250 km from the Tabuk source zone, expected PGA at Hegra from a M7.0 event is of order 0.02–0.06 g, sufficient to exceed $a_{s,crit}$ for any façade already in Phase C, but insufficient to destabilise intact façades whose safety factors largely exceed unity. Second, façades excavated directly into the Quweira Formation behave as single-block rock masses with seismic resistance higher than masonry-built structures and the historical damage records may reflect built construction rather than rock-cut monuments. The survival of intact façades is consistent with the model at $T_{50} = 615$ yr. The majority of south-facing façades are still in Phase A at any given time, and the observable 2000-year record samples survivors rather than the full population.

Finally, the presence of large-scale rockfalls and rockslides within the Al-'Ula–Hegra massifs (Beni et al., 2023; Gallego et al., 2023) provides landscape-scale corroboration of the Phase C completion mechanism. Many of these failures are morphologically consistent with model predictions: planar, surface-parallel detachments of limited thickness leaving smoothed, fresh rock surfaces, representing the cumulative outcome of thermal fatigue crack growth finalised by a seismic or hydrological trigger event. Their recurrence validates the inclusion of a stochastic seismic parameter in the Monte Carlo simulation and confirms that the Case 2 lateral crack geometry is a persistent, regionally significant mode of sandstone slope evolution.

6.8. Risk implications

6.8.1. Water as risk accelerator

The geomechanical data (20–40% tensile strength reduction by saturation; slake durability mass loss 15–100%; capillary rise 0.3–3.0 m at sample scale) and the fracture mechanics model converge on the conclusion that water availability is the highest acting risk variable at these sites. The double effect of moisture increase produces a 15-fold reduction in Phase A duration for the physically realistic condensation scenario, reducing $T_{brittle}$ from 1195 yr (dry base case) to approximately 80 yr. For sites with active capillary rise, Phase A durations collapse from centuries to decades. The Richards' plate extractor data quantify the moisture retention capacity of the Quweira Sandstone. Combined with the sensitivity curves in Fig. 23a, they provide a direct quantitative link between measurable hydrological field parameters (capillary rise height, seasonal humidity) and predicted failure timescales. The single most urgent laboratory measurement identified by this analysis is fracture toughness on a water-saturated core. If $K_{IC,wet} < 1.1 MPa{\cdot}m^{0.5}$ (i.e. nucleation threshold at $a_{obs} = 40$mm under mean climate), the system is in the brittle regime under mean conditions and requires immediate structural assessment.

6.8.2. Complementarity of analytical approaches

The fracture mechanics–Monte Carlo model and the finite element model are complementary. The fracture mechanics model resolves the spalling mechanism at the 1–100 mm scale, treating material variability probabilistically through the log-normal Paris coefficient distribution and producing risk-quantified survival curves for conservation decision-making. The FEM resolves global structural stability at the 1–100 m scale, capturing chamber–façade interaction, niche excavation effects, pillar stress concentrations, and thermo-mechanical coupling at the building scale. Both models are calibrated against the same Quweira Sandstone property set, ensuring parameter consistency. The measured post-saturation tensile strength of 0.9–3.2 MPa (single saturation), falling to 0.5–2.5 MPa after a complete wetting-drying cycle, and the Paris Law $K_{IC,wet}$ values provide the bridge between these frameworks. Conservation decisions require all three perspectives. The fracture model identifies which façades are approaching the Phase B brittle jump. The FEM identifies which chamber configurations are approaching plastic failure under weathering scenarios. The IR thermography provides the real-time observational link that updates both model predictions without physical intervention.

7. Conclusions

The integration of geomechanical characterisation, fracture mechanics modelling, infrared thermography, and finite element analysis at Hegra establishes a causal chain from diurnal thermal forcing to probabilistic slab detachment, with direct implications for rock-cut heritage beyond this site. Three-dimensional FEM confirms that under intact rock properties the tomb group is stable through the full excavation sequence (FS $>$ 5 for simplified geometry; FS $>$ 6 for Qasr al-Bint). Failure initiates at 60% cohesion reduction under partial saturation, consistent with the measured 20–40% water-induced tensile strength loss. The failure mechanism under layered saturation, corresponding to the field-observed capillary rise profile, shifts from deep sliding to a frontal plastic hinge at the façade base, driving forward collapse of the outer rock volume. This mode shift is consistent with the dominant pattern of façade thinning and forward collapse at Hegra, and identifies the capillary rise zone as the critical sector for structural intervention.

The surface-parallel crack geometry at 40–50 mm depth (Case 2), spanning the full façade width with the carved surface intact, is more hazardous than the conventional deepening model (Case 1). Under Case 1, K_I peaks at finite depth and decays, permitting crack arrest, consistent with corner cracks observed at the Al Farid façade. Under Case 2, K_I increases monotonically with crack height with no arrest mechanism, making a brittle jump to full façade height inevitable once $h_{brittle}$ is exceeded. This distinction has not been treated in previous weathering models and changes the risk calculation for rock-cut monuments.

Gravity is not the critical failure mechanism. Once the slab spans the full façade height, the safety factor against overturning is high. The critical trigger is seismic toppling at accelerations as low as 0.8%g, within the range of minor regional events and anthropogenic vibrations. Crack height, not surface deformation, is therefore the priority monitoring parameter. Water is the dominant risk variable through a double-jeopardy mechanism: morning condensation reduces K_{IC} and amplifies C, reducing Phase A duration by up to 15-fold, with active capillary rise collapsing failure timescales from centuries to decades. The spatial convergence of capillary moisture, wind abrasion, and thermal fatigue at the façade base creates a self-reinforcing feedback. Any management action increasing moisture access to the façade base activates this mechanism.

Infrared thermography is both a validation instrument and a monitoring tool. The 15.4 °C contrast at IGN55 independently validates effective diffusivity and maps crack size, whereas the diurnal polarity reversal distinguishes open-crack thermal decoupling from surface alteration. Systematic pre-dawn surveys could allow mapping of crack extent across the necropolis at negligible cost, enabling prioritisation of façades approaching the brittle threshold limit.

This study provides the first probabilistic lifetime estimate ($T_{50} = 615$ yr, P10 $\approx$ 300 yr) for rock-cut heritage under quantified environmental loading. The three-phase framework (i.e. A: subcritical fatigue, B: brittle jump, C: probabilistic trigger) requires four material parameters, one climate parameter, and façade height, making it transferable to Petra and to any rock-cut site in arid conditions where the ratio of brittle fracture size to façade height falls below 0.01. The single most urgent measurement for site-specific application is $K_{IC,wet}$, where values below 1.1 MPa·m$^{0.5}$ indicate a brittle-dominated regime requiring structural stabilisation rather than monitoring.

CRediT authorship contribution statement

Giovanni B. Crosta: Writing – original draft, Visualization, Software, Methodology, Investigation, Formal analysis, Conceptualization. **Giuseppe Dattola:** Software, Methodology. **Luca Cifeca Recinella:** Software. **Alberto Previati:** Writing – review & editing. **Serena Rigamonti:** Software, Investigation, Data curation.

Declaration of competing interest

The authors declare that they have no known competing financial interests or personal relationships that could have appeared to influence the work reported in this paper.

Acknowledgements

The authors wish to thank the Kingdoms Institute of the Royal Commission for AlUla (RCU). Field activities have been performed in the framework of the International Programme on Landslides IPL-259 project "Landslide Risk assessment in AlUla Archaeological sites – Kingdom of Saudi Arabia" coordinated by Claudio Margottini. José Ignacio Gallego Revilla from RCU is thanked for providing data and access to the sites. Laser scanning data were elaborated for the Kingdoms Institute of the RCU by Factum Foundation and kindly provided through the project. PANGEA SAS is thanked for supporting field work and sample shipping, and Daniele Spizzichino for his dedication to field work, organisation, and constructive discussions. Daniela Boldini, Tommaso Beni and William Frodella are thanked for their support during early field activities and on-site discussion. The authors gratefully acknowledge ESTIA Srl (Restauro Beni Culturali) and The Hegra Conservation Project for providing the two infrared thermography surveys of the IGN55 tomb and for the on-site valuable technical discussions. Nicoletta Fusi is thanked for supervising the geomechanical testing in the University of Milano-Bicocca laboratory.

Data availability

The authors do not have permission to share data.

References

Abdelwahed, M.F., El-Masry, N.N., Qaddah, A., Moufti, M.R., Alqahtani, F., 2020. Spatial distribution of the empirical peak ground motion in Western Saudi Arabia and its implication on Al-Madinah City. Arab. J. Geosci. 13 (5), 222.

Al-Arifi, N.S., Fat-Helbary, R.E., Khalil, A.R., et al., 2013. A new evaluation of seismic hazard for the northwestern part of Saudi Arabia. Nat. Hazards 69, 1435–1457. https://doi.org/10.1007/s11069-013-0756-1.

Al-Faqeer, H.M., 2009. Rainfall Analysis in the Al-'Ula Region. Ministry of Water and Electricity, Saudi Arabia.

Anderson, T.L., 2005. Fracture Mechanics: Fundamentals and Applications, 3rd edn. CRC Press, Boca Raton.

Atkinson, B.K., 1984. Subcritical crack growth in geological materials. J. Geophys. Res. 89 (B6), 4077–4114.

Atkinson, B.K., Meredith, P.G., 1987. The theory of subcritical crack growth with applications to minerals and rocks. In: Atkinson, B.K. (Ed.), Fracture Mechanics of Rock. Academic Press, London, pp. 111–166.

Beni, T., Boldini, D., Crosta, G.B., Frodella, W., Gallego, J.I., Lusini, E., Margottini, C., Spizzichino, D., 2023. Rock instabilities at the archaeological site of Dadan (Kingdom of Saudi Arabia). Landslides. https://doi.org/10.1007/s10346-023-02122-7.

Blocken, B., Derome, D., Carmeliet, J., 2013. Rainwater runoff from building façades: a review. Build. Environ. 60, 339–361.

Brantut, N., Heap, M.J., Meredith, P.G., Baud, P., 2013. Time-dependent cracking and brittle creep in crustal rocks: a review. J. Struct. Geol. 52, 17–43.

BRGM (1977) Hydrological reconnaissance of the Al-'Ula region. Bureau de Recherches Géologiques et Minières, report.

Carslaw, H.S., Jaeger, J.C., 1959. Conduction of Heat in Solids, 2nd edn. Oxford University Press.

Charles, R.J., 1958. Static fatigue of glass. J. Appl. Phys. 29 (11), 1549–1553.

Collins, B.D., Stock, G.M., 2016. Rockfall triggering by cyclic thermal stressing of exfoliation fractures. Nat. Geosci. 9, 395–400.

Cosentino, P.L., Capizzi, P., Martorana, R., Messina, P., Schiavone, S., 2011. From geophysics to microgeophysics for engineering and cultural heritage. Int. J. Geophys. 8. https://doi.org/10.1155/2011/428412, 428412.

Courbon, P., 2008. Les puits nabatéens de Madaʾin Ṣāliḥ (Arabie Saoudite). Arab. Archaeol. Epigr. 19 (1), 48–70.

D'Altri, A.M., de Miranda, S., Castellazzi, G., Glisic, B., 2023. Numerical modelling-based damage diagnostics in cultural heritage structures. J. Cult. Herit. 61, 1–12.

do Amaral Vargas, E., Velloso, R.Q., Chávez, L.E., Gusmão, L., Amaral, C.P., 2013. On the effect of thermally induced stresses in failures of some rock slopes in Rio de Janeiro, Brazil. Rock Mech. Rock. Eng. 46, 123–134.

Domej, G., Previtali, M., Castellanza, R., Spizzichino, D., Crosta, G.B., Villa, A., et al., 2022. High-resolution 3D FEM stability analysis of the Sabereebi Cave Monastery, Georgia. Rock Mech. Rock. Eng. 55 (8), 5139–5162.

Egartner, I., Sass, O., Viles, H., Dietzel, M., 2020. A multi-proxy investigation of moisture, salt, and weathering dynamics on a historic urban boundary wall in Oxford, UK. Stud. Conserv. 65 (3), 172–188.

Eppes, M.C., Keanini, R., 2017. Mechanical weathering and rock erosion by climate-dependent subcritical cracking. Rev. Geophys. 55, 470–508.

Eppes, M.C., Magi, B., Hallet, B., Delmelle, E., Mackenzie-Helnwein, P., Warren, K., Swami, S., 2016. Deciphering the role of solar-induced thermal stresses in rock weathering. Bulletin 128 (9–10), 1315–1338.

Franzen, C., Mirwald, P.W., 2004. Moisture content of natural stones: static and dynamic equilibrium with atmospheric humidity. Environ. Geol. 46, 391–401.

Franzoni, E., 2017. State-of-the-art on methods for reducing rising damp in masonry. J. Cult. Herit. 108, 257–269.

Gallego, J.I., Margottini, C., Perissé Valero, I., Spizzichino, D., Beni, T., Boldini, D., et al., 2023. Rock slope instabilities affecting the AlUla archaeological sites (KSA). In: Progress in Landslide Research and Technology, 2. Springer, pp. 413–429.

Goudie, A.S., 2013. Arid and Semi-Arid Geomorphology. Cambridge University Press.

Guerin, A., Jaboyedoff, M., Collins, B.D., et al., 2019. Detection of rock bridges by infrared thermal imaging and modeling. Sci. Rep. 9, 13138.

Hashemi, M., Khabbazi Basmenj, A., Banikheir, M., 2018. Engineering geological and geoenvironmental evaluation of UNESCO World Heritage Site of Meymand rock-hewn village, Iran. Environ. Earth Sci. 77 (1), 3.

Heinrich, K., 2008. Diagnosis of weathering damage on rock-cut monuments in Petra, Jordan. Environ. Geol. 56, 643–675.

ICOMOS, 2008. Advisory Body Evaluation for the Hegra Archaeological Site. https://whc.unesco.org/en/list/1293/documents/.

Jaussen, A., Savignac, R., 1914. Mission Archéologique en Arabie II. Publications de la Société des Fouilles (Archéologiques).

Kachanov, M., 1987. Elastic solids with many cracks: a simple method of analysis. Int. J. Solids Struct. 23 (1), 23–43.

Laity, J.E., 2011. Wind Erosion in Drylands. In: Thomas, D.S.G. (Ed.), Arid Zone Geomorphology. Wiley.

Markowska, M., Vonhof, H.B., Groucutt, H.S., Breeze, P.S., Drake, N., Stewart, M., Haug, G.H., 2025. Recurrent humid phases in Arabia over the past 8 million years. Nature 640 (8060), 954–961.

Martel, S.J., 2017. Progress in understanding sheeting joints over the past two centuries. J. Struct. Geol. 94, 68–86.

Martinez, F., Cochran, J.R., 1988. Structure and tectonics of the northern Red Sea. Tectonophysics 150 (1–2), 1–31.

Martínez-Garrido, M.I., Fort, R., Gómez-Heras, M., Valles-Iriso, J., Varas-Muriel, M.J., 2018. A comprehensive study for moisture control in cultural heritage using non-destructive techniques. J. Appl. Geophys. 155, 36–52.

McCarthy, J., 2014. Multi-image photogrammetry as a practical tool for cultural heritage survey and community engagement. J. Archaeol. Sci. 43, 175–185.

Meng, Z., Fan, F., Cui, X., Tao, S., Cao, Y. (2021) Numerical modeling and stability analysis of surrounding rock of Yuanjue Cave. Geofluids, 2021, 665227.21.

Mineo, S., Pappalardo, G., 2019. Infrared thermography as an innovative and non-destructive solution to quantify rock porosity. Int. J. Rock Mech. Min. Sci. 115, 99–110.

Nara, Y., Morimoto, K., Hiroyoshi, N., Yoneda, T., Kaneko, K., Benson, P.M., 2012. Influence of relative humidity on fracture toughness of rock: implications for subcritical crack growth. Int. J. Solids Struct. 49 (18), 2471–2481.

Nara, Y., Morimoto, K., Yoneda, T., Hiroyoshi, N., Kaneko, K., 2011. Effects of humidity and temperature on subcritical crack growth in sandstone. Int. J. Solids Struct. 48 (7–8), 1130–1140.

Nara, Y., Nakabayashi, R., Maruyama, M., Hiroyoshi, N., Yoneda, T., Kaneko, K., 2014. Influences of electrolyte concentration on subcritical crack growth in sandstone in water. Eng. Geol. 179, 41–49.

Nehmé, L., 2015. Les tombeaux nabatéens de Hégra (Épigraphie et archéologie 2). AIBL/De Boccard, Paris, 2015, vol. 1 texte (433 p.), vol. 2, catalogue et planches (232 p. de 249 pl.), ISBN : 978-2-87754-328-6.

Noël, C., Baud, P., Violay, M., 2021. Effect of water on sandstone's fracture toughness and frictional parameters: Brittle strength constraints. Int. J. Rock Mech. Min. Sci. 147, 104916.

Orr, S., Fusade, L., Young, M., 2020. Moisture monitoring of stone masonry: a comparison of microwave and radar on a granite wall and a sandstone tower. J. Cult. Herit. 41, 61–73.

Paradise, T.R., 2013. Assessment of tafoni distribution and environmental factors on a sandstone djinn block above Petra, Jordan. Appl. Geogr. 42, 176–185.

Paris, P., Erdogan, F., 1963. A critical analysis of crack propagation laws. J. Basic Eng. 85 (4), 528–533.

Rihosek, J., Bruthans, J., Masin, D., Filippi, M., Carling, G.T., Schweigstillova, J., 2016. Gravity-induced stress as a factor reducing decay of sandstone monuments in Petra, Jordan. J. Cult. Herit. 19, 415–425.

Ruedrich, J., Bartelsen, T., Dohrmann, R., Siegesmund, S., 2011. Moisture expansion as a deterioration factor for sandstone used in buildings. Environ. Earth Sci. 63 (7–8), 1545–1564.
Safonov, A., Filippi, M., Mašín, D., Bruthans, J., 2020. Numerical modeling of the evolution of arcades and rock pillars. Geomorphology 365, 107260.
Saleh, M.M., El-Sorogy, A.S., Youssef, M., Al-Kahtany, K., 2021. Evaluation of geoenvironmental hazards at Qasr Al-Farid tomb, Mada'in Saleh, Saudi Arabia. Arab. J. Geosci. 14, 47.
Salisbury, J.W., D'Aria, D.M., 1992. Emissivity of terrestrial materials in the 8–14 μm atmospheric window. Remote Sens. Environ. 42 (2), 83–106.
Sass, O., Viles, H., 2010. Wetting and drying of masonry walls: 2D-resistivity monitoring of driving rain experiments on historic stonework in Oxford, UK. J. Appl. Geophys. 70, 72–83.
Sass, O., Viles, H., 2022. Heritage hydrology: a conceptual framework for understanding water fluxes and storage in built and rock-hewn heritage. Herit. Sci. 10 (1), 66.
Siegesmund, S., Durrast, H., 2011. Physical and mechanical properties of rocks. In: Siegesmund, Snethlage (Eds.), Stone in Architecture. Springer, Heidelberg.
Sokolov, V., Zahran, H.M., Youssef, S.E.H., et al., 2017. Probabilistic seismic hazard assessment for Saudi Arabia using spatially smoothed seismicity. Bull. Earthq. Eng. 15, 2695–27.235.
Tada, H., Paris, P.C., Irwin, G.R., 2000. The Stress Analysis of Cracks Handbook, 3rd edn. ASME Press.
Van Genuchten, M.T., 1980. A closed-form equation for predicting the hydraulic conductivity of unsaturated soils. Soil Sci. Soc. Am. J. 44 (5), 892–898.
Vincent, P., 2008. Saudi Arabia: an environmental overview. CRC Press, 332 pp.
Wahbi, A.M., 2014. Sedimentological and Stratigraphic Studies of the Cambro-Ordovician Succession in Northwest Saudi Arabia [MSc Thesis]. King Fahd University of Petroleum and Minerals.
Wang, Y., Hao, Z., Zhang, H., 2024. In situ investigation of the moisture distribution and deterioration of the façade of limestone rock-hewn heritage. Rock Mech. Rock. Eng. 57, 27.255–27.262.
Weatherspark, 2020. Climate and Average Weather Year Round in Al-'Ula. https://weatherspark.com/.
Wedekind, W., Ruedrich, J., Siegesmund, S., 2011. Conservation inventory systems for monitoring and protection of cemeteries and tomb façades. In: Jardins de Pierres: Conservation de la Pierre dans les Parcs, Jardins et Cimetières, p. 181.
Weissbrod, T., Sneh, A., 2002. Sedimentology and paleogeography of the Late Precambrian–Early Cambrian arkosic and conglomeratic facies in the southern Levant. . Geol. Surv. Isr., Bull. 87.
Young, R., Young, A. (2012) Sandstone Landforms. Springer Series in Physical Environment, Springer-Verlag Berlin Heidelberg, 163 pp.